

SURFACE INDUCED DISSOCIATION (SID) AS A TOOL FOR PROBING
HALOGENATED ALKANETHIOLATE SELF-ASSEMBLED MONOLAYER FILMS
AND REACTIVITY OF POLYATOMIC IONS

by

Zhuhua Qi

A Thesis Submitted to the Faculty of the
DEPARTMENT OF CHEMISTRY
In partial Fulfillment of the Requirements
For the Degree of
MASTER OF SCIENCE
In the Graduate College
THE UNIVERSITY OF ARIZONA

2005

ACKNOWLEDGMENTS

I would like to thank my research advisor, Vicki H. Wysocki, for her guidance, encouragement, and patience during my graduate study.

I would also like to thank previous and current group members (Dr. Facundo Fernandez, Dr. Krishnamoorthy Kuppannan, Dr. Selvan Ravindran, Dr. Darrin Smith, Dr. Lori Smith, Dr. Yingying Huang, Dr. Amy Hilderbrand, Dr. Richard Beardsley, Dr. Kristin Hermann, Dr. Chaminda Gamage, Qingfen Zhang, Xi Yang, Karen Bryden Joyce, Guilong Cheng, Asiri Galhena, Xiujuan Wen, Guanhong Tan, Samantha Wickramasekara, Chris Jones, Yimin Hua, Lei Shi, Sung Hwan Yoon, Brittany Perkins, Tanya Grumbine) for their friendship, the help with my research, shared interests and frustrations.

I also had the chance to work in the Mass Spectrometry Facility where Dr. Arpad Somogyi, Dr. Linda Brechi, and Mark Malcomson not only taught me academic knowledge but also gave me a lot of help and encouragement.

I would like to thank Dr. Ron Wysocki in the Chemical synthesis Laboratory for synthesizing the compounds for my research, Amy Graham and Dana Alloway for providing the UPS data, Dr. Nadine gruhn for providing the gas-phase UPS data and helpful discussions, and Dr. Kenneth Nebesny and Mr. Paul Lee in the LESSA Facility for helping with the knowledge and experiment of UPS, and Dr. Mary Wirth for the use of FT-IR instrument .

And, finally, I would like to thank my family for their love and support.

TABLE OF CONTENTS

LIST OF FIGURES	6
LIST OF TABLES	12
ABSTRACT.....	13
Chapter 1. Introduction	14
1.1 Ion-surface collision in tandem mass spectrometry.....	14
1.1.1 Tandem mass spectrometry	14
1.1.2 Ion activation methods in tandem mass spectrometry.....	15
1.1.3 Important processes during low energy ion-surface collision.....	18
1.1.4 Soft landing	23
1.2 Self-assembled monolayers (SAMs).....	24
1.2.1 What are SAMs?	24
1.2.2 SAMs of thiol on Au	25
1.3 Questions to be answered in this thesis.....	27
Chapter 2. Instrumentation and Experimental Methods	29
2.1 Instrumentation	29
2.1.1 Dual-quadrupole SID mass spectrometer.....	29
2.1.2 Ultraviolet photoemission spectroscopy (UPS)	31
2.1.3 Fourier transform infrared spectroscopy (FT-IR)	36
2.1.4 Contact angle.....	37
2.2 Organic thin films on Au substrate	39
2.2.1 Synthesis and listing of SAMs used in the thesis.....	40

TABLE OF CONTENTS - *continued*

2.2.2 Preparation of SAM surfaces	44
Chapter 3. Ion Surface Collision as a Tool for Probing both Projectile Ions and Halogen Terminated SAM films	46
3.1 Introduction.....	46
3.2 Results and discussion	51
3.2.1 Conversion of kinetic energy into internal energy for projectile ions.....	58
3.2.2 Electron transfer	66
3.2.3 Ion-surface reactions	77
3.3 Conclusions.....	82
Chapter 4. Development of Soft Landing as a Method for Separation.....	84
4.1 Introduction.....	84
4.2 Experimental.....	87
4.3 Soft landing of YGGFLR on different SAMs.....	87
4.4 Conclusion	91
Chapter 5. Summary and Future Directions	94
REFERENCES	98

LIST OF FIGURES

- FIGURE 1.1. Schematic of tandem mass procedure14
- FIGURE 1.2. Comparison of activation process between SID “sudden” and multiple collision CID “slow heating”. Figure was modified from reference 20. Copyright permission from the publisher (ACS).....17
- FIGURE 1.3. Energy-resolved tandem mass spectra of $W(CO)_6$ obtained by using (a) SID and (b) single collision CID with Ar at 10-100 eV and with He at 8keV. Figure was modified from reference 32. Copyright permission from the publisher (Elsevier)19
- FIGURE 1.4. Processes happening during a low energy ion-surface collision: (a) energy transfer and dissociation, (b) electron transfer, (c) atom/group transfer, (d) chemical sputtering. Note: The angles indicated by arrows do not represent the scattering angles of the specific species20
- FIGURE 1.5. Structure model of the *n*-alkanethiolate adlayer on gold lattice. (a) An alkanethiol molecule with a tilt angle of θ relative to the surface normal and a rotational angle ψ along the molecular axis. (b) is a $(\sqrt{3} \times \sqrt{3})R30^\circ$ structure where the sulfur atoms (light gray circles) are positioned in the 3-fold hollows of gold lattice (white circles, $a = 2.88 \text{ \AA}$). (c) is a $c(4 \times 2)$ superlattice structure marked by dashed line. The molecular S–C axis, is strongly tilted ($45^\circ - 53^\circ$) and hydrogen atoms are

LIST OF FIGURES – *Continued*

twisted with respect to those in the other molecule. Figure was adapted from reference 77. Reprinted with permission from Structure and Energetics of Alkanethiol Adsorption on the Au (111) Surface , by Yashar Yourdshahyan, Andrew M. Rappe. Copyright 2005, American Institute of Physics.....	28
FIGURE 2.1. Dual quadrupole SID tandem mass spectrometer. Figure adapted from reference 79.....	30
FIGURE 2.2. Schematic representation of the XPS. Figure was modified from reference 80.....	33
FIGURE 2.3. schematic of the <i>Kratos</i> Ultra photoelectron spectrometer. Figure modified from reference 77.....	34
FIGURE 2.4. Depiction of a drop of liquid on a hydrophilic surface. γ_{SV} represents the free energy of the solid-vapor interface, γ_{LV} represents the free energy of the liquid-vapor interface, and γ_{SL} represents the free energy of the solid-liquid interface	38
FIGURE 3.1. Comparison of even (left two chains, 12 carbons) and odd (right two chains, 11 carbons) chain lengths hydrocarbon SAMs. Figure was drawn by ChemDraw 3D	52
FIGURE 3.2. Side view of idealized structure for C12F1 (CF ₃ terminal group), C12Cl (CH ₂ Cl terminal group), C12Br (CH ₂ Br terminal group), and C12 (CH ₃	

LIST OF FIGURES – *Continued*

- terminal group) SAMs. Figure was drawn by ChemDraw 3D54
- FIGURE 3.3. Methyl and methylene stretching region of the reflection absorption FT-IR spectra of C14F1, C12Cl, C12Br, and C12 surfaces55
- FIGURE 3.4. Illustration of different dipole orientations of C12Br and C11Br surfaces57
- FIGURE 3.5. Product ion spectra with benzene projectile ion (m/z 78) colliding with (a) C14F1, (b) C12Cl, (c) C12Br, and (d) C12 surfaces at 30 eV collision energy. Product ions with m/z greater than m/z 78 correspond to addition products formed by reaction of the projectile with surface chains59
- FIGURE 3.6. Product ion spectra with pyrazine projectile ion (m/z 80) colliding with (a) C14F1, (b) C12Cl, (c) C12Br, and (d) C12 surfaces at 20 eV collision energy. The peak at m/z 81 is the hydrogen addition product formed by abstraction of hydrogen atom from the SAM films, and that at m/z 54 corresponds to the loss of HCN60
- FIGURE 3.7. Comparison of mean energy deposition E_m (relative to the collision energy 30 eV) for C12Br, C12F10, C14F1, C12Cl and C12 surfaces with benzene and $W(CO)_6$ as projectile ions. (a) original values calculated by extended deconvolution method for benzene⁽⁴⁰⁾ and by algorithm for $W(CO)_6$.⁽³²⁾ (b) original value for benzene and adjusted value for $W(CO)_6$ by adding the first appearance energy difference between benzene (4.6 eV

LIST OF FIGURES – *Continued*

-) and $W(CO)_6$ (1.2 eV) from values shown in (a).....61
- FIGURE 3.8. Plots of mean internal energy deposition versus terminal group mass of the $C_{12}F_{10}$, $C_{14}F_1$, $C_{12}Cl$, $C_{12}Br$, and C_{12} surfaces assuming that the terminal group is defined by the terminal carbon and its attached atoms.
(a) benzene projectile ion (b) $W(CO)_6$ projectile ion.....63
- FIGURE 3.9. Product ion spectra with $W(CO)_6^+$ projectile ion colliding with (a) $C_{14}F_1$, (b) $C_{12}Cl$, (c) $C_{12}Br$, and (d) C_{12} surfaces at 30 eV collision energy64
- FIGURE 3.10. ChemDraw 3D demonstration of difference between C_{11} and C_{12} diluted $C_{12}Br$ surfaces. $C_{12}Br:C_{11}$ (50:50) surface has more exposed CH_2Br group and less exposed CH_3 group than $C_{12}Br:C_{12}$ (50:50) surface. More exposed is defined as greater height difference between adjacent groups.67
- FIGURE 3.11. Comparison of estimated average internal energy deposited into (a) benzene and (b) $W(CO)_6$ projectile ions on C_{12} and C_{11} diluted $C_{12}Cl$ (i) and $C_{12}Br$ (ii) surfaces as a function of their concentrations in solution. C_{11} diluted surfaces always show higher energy deposition than the C_{12} diluted ones. Points are connected with best fit lines to highlight the difference between C_{11} and C_{12} diluted surfaces. Diamonds represent C_{12} diluted surfaces, squares represent C_{11} diluted surfaces68
- FIGURE 3.12. Total ion current surviving collision with $C_{14}F_1$, $C_{12}Cl$, $C_{12}Br$, and C_{12}

LIST OF FIGURES – *Continued*

surfaces using pyrazine projectile ion at 20 eV collision energy.....	69
FIGURE 3.13. UPS spectra for clean Au and C12Cl, C12Br, C12 surfaces on Au foil....	71
FIGURE 3.14. Relationship between the total ion current for benzene projectile ion and (a) surface ionization energy and (b) surface dipole calculated from UPS spectra. Curves indicate the best exponential fit obtained for the data.....	74
FIGURE 3.15. Relationship between the total ion current for pyrazine projectile ion and (a) surface ionization energy and (b) surface dipole calculated from UPS spectra. Curves indicate the best exponential fit obtained for the data.....	75
FIGURE 3.16. Gas-phase UPS spectra for C12F10, C12, C12Cl, and C12Br surfaces. The sharp peak at low IE arises from the ionization of the sulfur lone pair orbitals (marked by (*))	76
FIGURE 3.17. The comparison of hydrogen addition quotient (HRQ) for C12F10, C14F1, C12Cl, C12Br, and C12 surfaces	79
FIGURE 3.18. Product ion spectra obtained by colliding CD ₃ ⁺ projectile ion with C14F1, C12Cl, C12Br, and C12 surfaces at 30 eV collision energy.....	81
FIGURE 4.1. Schematic diagram demonstration of the lens voltages employed in soft landing experiment at both 5 eV and 30 eV collision energies	90
FIGURE 4.2. MALDI spectra for YGGFLR soft-landed on a C11OH surface at (a) 5 eV	

LIST OF FIGURES – *Continued*

and (b) 30 eV and subsequently collected by a solvent rinse. The peak at
m/z 712 is the (YGGFLR-H)⁺ ion, peaks at lower m/z range are matrix
peaks93

LIST OF TABLES

TABLE 2.1.	Thiol compounds and abbreviations for SAM films used in this research	41
TABLE 3.1.	Water advancing contact angle for C12F10, C14F1, C12Cl, C12Br, and C12 surfaces.....	56
TABLE 3.2.	Ionization energy, interface dipole (from UPS), and TIC for C12F10, C14F1, C12Cl, C12Br, and C12 surfaces.....	77
TABLE 4.1.	Typical lens voltages used in soft landing experiment on the Extrel 4000 instrument	89

ABSTRACT

Low energy (< 100 eV) ion-surface collisions of small polyatomic ions on halogen terminated alkanethiolate self-assembled monolayers were used to probe both the structure and the property of the organic thin films and the nature of the polyatomic ions.

In Chapter 3, the conversion of a portion of the projectile ion's kinetic energy to internal energy is proven to be dominantly determined by the mass of the terminal group. The main factor that determines the electron transfer process is the orientation and magnitude of the interface dipole instead of their ionization energy of the surface. Ion-surface reactions are predominantly determined by the nature of the film's terminal group.

In chapter 4, a peptide, YGGFLR, was used to perform soft landing on three different self-assembled monolayers at two collision energies, 5 eV and 30 eV. Successful soft landing was achieved on all three surfaces at only 30 eV collision energy.

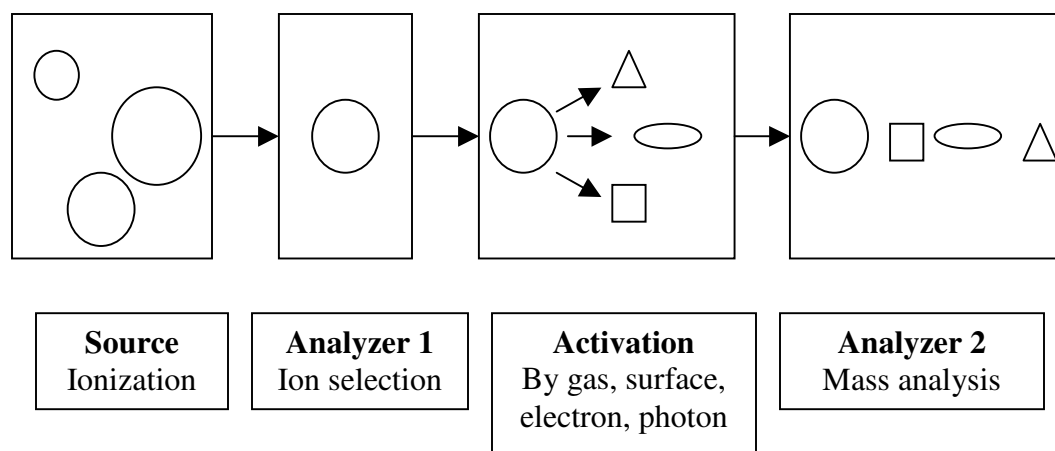
Chapter 1. Introduction

1.1 Ion- surface collision in tandem mass spectrometry

1.1.1 Tandem mass spectrometry

In tandem mass spectrometry, two stages of mass analysis are combined. In the common MS/MS experiment, the first mass analyzer is used to selectively pass one ion with a selected mass/charge ratio into the reaction region where the selected precursor ion is activated and dissociated. The second mass analyzer records the mass to charge ratio for the precursor ions and the fragment ions. Figure 1.1 shows the basic MS/MS procedure. Tandem mass spectrometry is a powerful analytical tool that provides information about structure, reactivity, proton affinity, bond strengths, and has numerous chemical and biological applications.^(1,2) The ion activation step is crucial to the experiments and determines the extent of fragmentation and types of dissociation products.

Figure 1.1 Schematic of tandem mass spectrometry product ion experiment.



1.1.2 Ion activation methods in tandem mass spectrometry

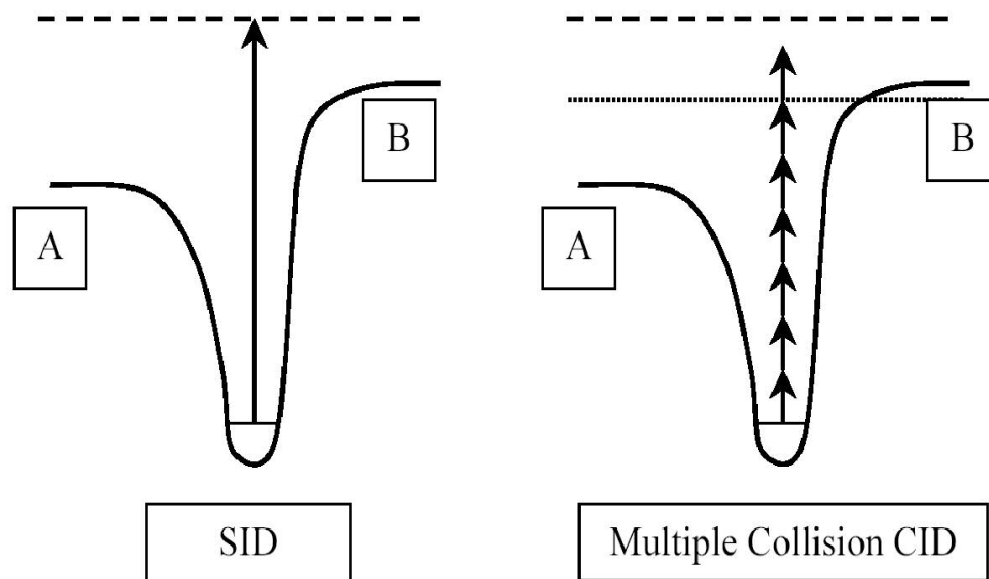
Development of ion activation methods has come through several stages. Early experiments used metastable ion decomposition. In this method, some of the molecular ions formed in the source have sufficient internal energy to fragment spontaneously before entering the mass analyzer. However, there is no control over the fragmentation, and the characterization ability is limited by the complicated instrumentation and scans.

⁽³⁾ Collision-induced dissociation (CID) was then introduced and is still the most commonly employed activation method in tandem mass spectrometry. ^(4,5) CID involves a collision between precursor ion and a neutral target gas, often Ar, He, N₂ or some combination of gases. Part of the precursor ion's translational energy is converted into its internal energy which results in fragmentation. Based on the translational energy of the precursor ion, CID can be divided into two categories: low energy CID, with collision energies of 10-100eV, and high energy CID, with collision energies in the kiloelectronvolt range. Since low energy CID is commonly used in quadrupole, ion trap, and Fourier-transform ion cyclotron resonance (FT-ICR) instruments⁽³⁾ and is more closely related to the low energy SID used in the research described in this thesis, it will be discussed in more detail. High energy CID is often used in sector and TOF (time-of-flight) /TOF instruments and will not be discussed here. Energy deposition into projectile ions in low energy CID is determined by both the nature of the target gas and the pressure in the collision cell. More energy is deposited into the precursor ion and more products are obtained with the use of target gases with higher mass. Higher gas pressures increase both the number of ions undergoing collision and the collision frequency of an individual

ion with neutral gas. In addition, the fragments can be further activated by multiple collisions and dissociated. Because the ion-gas interaction time is in the $\sim 10^{-13} - 10^{-14}$ s range which matches the bond vibration time,⁽⁶⁾ ion excitation is mostly vibrational.

Although CID is the most widely used activation method in mass spectrometry, many other new activation methods have been developed such as surface-induced dissociation (SID),^(7,8) electron-capture dissociation (ECD),⁽⁹⁾ infrared multiphoton dissociation (IRMPD),⁽¹⁰⁾ and blackbody infrared radiative dissociation (BIRD).⁽¹¹⁾ Because the research performed for this thesis mainly involves low energy SID, SID will be addressed in detail. SID was first developed in the 1970s and most of the pioneering studies were performed in Cook's laboratory.^(7,8,12-16) Many other research groups have also been involved in SID studies including the Wysocki group⁽¹⁷⁻¹⁹⁾, Futrell group,^(4,20) Hase group,^(21,22) Hanley group,^(23,34) McLafferty group,^(25,26) Whetten group,^(27,28) and Wilkins group.^(29,30) SID is a process where incident analyte ions collide elastically and inelastically with a surface. SID is a one-step or "sudden" activation while multiple collision CID is a step-wise activation⁽²⁰⁾ as shown in Figure 1.2. (Figure modified from reference 20) Compared with CID, SID converts more of the projectile ions' kinetic energy into projectile internal energy.^(31,32) Although it is generally believed that SID provides a more narrow internal energy distribution than CID,^(31,32) recent studies by Laskin *et al.* demonstrated that SID and multiple collision CID have similar internal energy distributions.⁽²⁰⁾ The merits of SID are especially useful for determining dissociation mechanisms of large molecules such as protonated peptides and proteins,^(33,34) and for isomer distinction when comparing relative intensities in energy-

Figure 1.2. Comparison of activation process between SID “sudden” and multiple collision CID “slow heating”. Figure was modified from reference 20. Copyright permission from the publisher (ACS).



resolved mass spectrometry.⁽³⁵⁾ The example in Figure 1.3 clearly demonstrates the difference in internal energy deposition between single collision CID and SID. SID is also advantageous over CID for the fact that it does not require additional vacuum system in the reaction region since no extra gas is introduced.

Low energy ion-surface collisions (10-100 eV) must be differentiated from either secondary ion mass spectrometry (SIMS), which uses high energy ion-surface collision (keV) where momentum sputtering is the major process,^(36,37) or low energy “soft-landing” where selected ions are deposited on the surface intact.^(38,39)

1.1.3 Important processes during low energy ion-surface collision

There are at least four processes happening during the ion-surface collision including (i) conversion of the projectile ion’s collision energy into its internal vibrational energy, (ii) electron transfer from the metal substrate to the projectile ion, (iii) atom/group transfer from the surface to the projectile ion which gives reaction products, and (iv) chemical sputtering (Figure 1.4).

(i) Conversion of projectile ion’s collision energy into internal energy (T→V)

During ion-surface collision, a portion of the projectile ion’s kinetic energy is converted into projectile internal vibrational energy and unimolecular dissociation occurs. The conversion efficiency depends on both the collision energy^(40,41) and the nature of the surface used.⁽⁴⁰⁻⁴³⁾ The deposited internal energy increases almost linearly with collision energy in the useful low energy range (20-60 eV).^(40,41) SAMs with different terminal groups have been reported to show different amount of energy transfer to projectile ions. With $W(CO)_6$ as the projectile ion, it was found that 12% kinetic to internal energy

Figure 1.3 Energy-resolved tandem mass spectra of $W(CO)_6$ obtained by using (a) SID and (b) single collision CID with Ar at 10-100 eV and with He at 8keV. Figure was modified from reference 32. Copyright permission from the publisher (Elsevier).

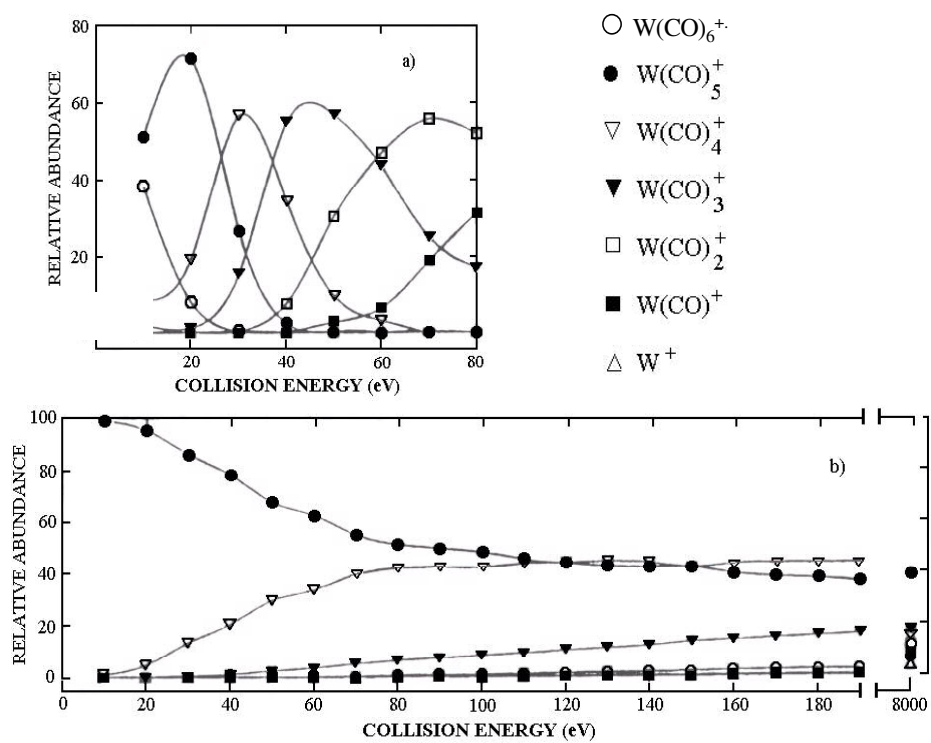
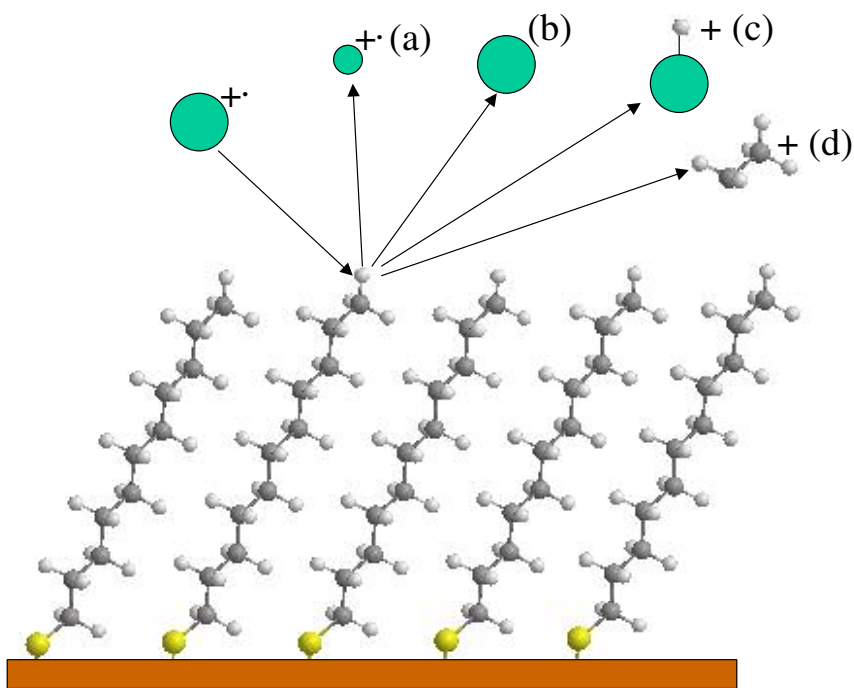


Figure 1.4 Processes happening during a low energy ion-surface collision: (a) energy transfer and dissociation, (b) projectile ion neutralization, (c) atom/group transfer, (d) chemical sputtering. Note: The angles indicated by arrows do not represent the scattering angles of the specific species.



transfer happened on C18 alkanethiol SAM compared to 19% on a C12F10 surface.⁽⁴²⁾ Later Cooks' group reported the conversion of 15% internal energy for an alkanethiolate monolayer and 24% for fluorinated monolayer when using ferrocene as the projectile ion.⁽⁴³⁾ By employing the extended deconvolution method for benzene molecular ions, Vekey *et al.* obtained the T→V value of 17% for C18 monolayer and 28% for 2-(perfluorooctyl)-ethanethiolate monolayer.⁽⁴⁰⁾ More recently Smith *et al.* compared the energy deposition on various hydrocarbon and partially fluorinated alkanethiol SAMs with benzene projectile ion. They reported that the internal energy deposition values were 19%, 26%, 27% and 28% for C16, C16F1, C16F2, and C16F10 surfaces, respectively. Their conclusion is that the terminal group mainly determines energy transfer and the mass of the terminal group is the most direct contributor to the extent of T→V.⁽⁴¹⁾ Besides terminal mass, there are several other factors that have been proposed to determine the amount of energy deposition including surface rigidity and the mass ratio of projectile to surface terminal group. More specific background and discussion about these contributing factors will be presented in Chapter 3.

(ii) Electron transfer from the metal substrate to the projectile ion

During ion-surface collision some of the projectile ions can obtain electrons from the metal substrate to form neutral species. SAM films serve as electron transfer barriers which decreases the neutralization of the incoming ions and enhances the ion current that reaches the detector compared to collisions with bare metal surfaces.⁽⁴²⁾ In contrast to an insulating surface, charge accumulation does not occur on the SAM film.⁽⁴⁴⁾ The properties that determine the extent of ion neutralization have been studied and several

possible factors have been reported.^(41,42,45) While extent of neutralization roughly tracks with the difference between the ionization energy of the surface and the recombination energy of the projectile ion,^(41,42) it may be the vacuum-surface interface dipole that is the main determinant.⁽⁴⁶⁾ The instrument utilized in this research enables the measurement of total ion current survival from the collision and helps to investigate this question. Chapter 3 provides more investigation on electron transfer through the SAM film. SAM surfaces with different ionization energy and interface dipoles were studied and it was found that the interface dipole is the main determinant for electron transfer through the SAM films.

(iii) Atom/group transfer

Collisions of ions with the surface may result in a reaction between the projectile ion and the organic film, especially for odd-electron projectiles.^(42,47,48) Abstraction of H and/or C_nH_m from hydrocarbon surfaces and F abstraction from fluorinated surfaces by small organic projectile ions have been reported.^(41,42,47,49,50) Studies by the Wysocki group have shown that ion-surface reactions happen predominantly but not exclusively from the uppermost portion of the film while the underlying $-CH_2-$ or $-CF_2-$ play a minor role.^(41,47,49,50) Intensities of the reaction products are very sensitive to the chain lengths of organic films and show odd-even effects.^(41,51) It has been proved that SAM films with odd chain lengths show higher abundance of hydrogen addition products while SAM films with even chain lengths show more methyl addition products. This provides a clear demonstration of the terminal group orientation differences between odd and even chain lengths. Specifically, the last C-C bonds of the odd-chain-length SAMs are more parallel

to the surface plane which enables one hydrogen atom on the terminal methyl and both hydrogen atoms on the first underlying methylene more reactive positions compared to even chain lengths. Conversely, the last C-C bonds of the even-chain-length SAMs are more perpendicular to the surface plane which allows the methyl carbon to be more reactive sites.⁽⁵¹⁾

(iv) Chemical sputtering

Chemical sputtering happens when the impingement of projectile ions at the surface causes ejection of secondary ions. Ionization of the organic thin film has been attributed to the charge exchange between the projectile ion and the organic surface.⁽⁵²⁾ Sometimes chemical sputtering can happen during low energy ion-surface collision processes and can be useful in the characterization of surface composition. It needs to be pointed out that this chemical sputtering process should be differentiated from SIMS because it uses low energy (< 100 eV) projectile ions, and the sputtering ion signals increase with collision energy and are dependent on the nature of the projectile used.⁽⁸⁾ Since chemical sputtering is not the dominant process in the research performed in this thesis, it will not be addressed in detail.

1.1.4 Soft landing

Soft landing is defined as the intact deposition of gas phase polyatomic ions onto an appropriate surface at low collision energy.⁽³⁸⁾ Low collision energies are preferred to suppress the surface-induced dissociation as well as ion-surface reactions. It should also be pointed out that too low an energy results in difficulties in focusing the ion beam and an increase in reflection. More information on soft landing will be provided in Chapter 4.

1.2 Self-assembled monolayers (SAMs)

Self-assembled monolayers on gold surfaces are useful model surfaces for the study of ion-surface collisions because the chemical composition of the terminal functional groups can be easily tailored. The SAMs used in this research are alkanethiolate films with different terminal groups on Au to investigate the effect of terminal group chemical and electronic properties on the important processes happened during ion-surface collisions.. The complete list of the SAMs used and the preparation of SAMs are presented in Chapter 2.

1.2.1 What are SAMs?

Self-assembled monolayers are ordered molecular assemblies that are formed spontaneously by the adsorption of molecules with specific headgroups that can bond to the substrate. SAMs have attracted extensive interest due to the following reasons⁽⁵³⁾:

- (i) preparation is easy, usually only requires incubating in the solution,
- (ii) surface properties can be easily tuned by changing the structure and chemical composition of the molecules,
- (iii) SAMs can be used as building blocks,
- (iv) nanoscale lateral structure can be formed

Physical and chemical properties of self-assembled monolayers have been examined by many different and complementary surface science techniques, both *ex situ* and *in situ*, such as UHV techniques (XPS⁽⁵³⁾, AES⁽⁵⁴⁾), spectroscopies (IR, Raman^(55,56)), and scanning probe microscopies (SPM) (STM, AFM^(53,57)). The large amount of information on SAMs obtained from these techniques opens many perspectives on their applications.

Indeed, SAMs have found wide applications in fields such as protective coatings,⁽⁵⁸⁾ adhesion,⁽⁵⁹⁾ biosensors,⁽⁶⁰⁻⁶²⁾ electric devices,⁽⁶³⁻⁶⁵⁾ and nanotechnology.^(66,67)

1.2.2 SAMs of thiol on Au

Although many substrates such as metals, oxides, and semiconductors can be used in forming SAMs, gold is still the standard due to its unique characteristics listed below.⁽⁶⁸⁾ Gold is easy to obtain either as a thin film or as crystals. It is easy to pattern by lithographic methods such as photolithography and chemical etchants. Also gold is relatively inert and does not react with most chemicals and oxygen in the air. It has been one of the most widely used substrates for many spectroscopies and analytical techniques including surface plasma resonance (SPR) spectroscopy, ellipsometry, quartz crystal microbalance (QCM). Finally, gold is compatible with cells so that cells adhere and function on gold surfaces without evidence of toxicity, which is beneficial for biological studies. The SAMs most directly related to the current research are thiols on Au, this type of SAMs will be addressed in more detail.

Gold binds the sulfur of the alkanethiols with a high affinity but does not react with the chain or the terminal groups. This high affinity also enables thiols to readily displace adventitious materials from the surface.⁽⁶⁸⁾ Factors that affect the SAM structure and formation rate are solvent, temperature, concentration of thiol solution, preparation time, purity and structure of thiol, oxygen concentration in solution, and substrate cleanliness.⁽⁶⁸⁻⁷²⁾ Most studies show that SAMs formed in thiol solutions in millimolar concentration ranges obtain *average* properties (wettability, dense coverage, and, to a large extent, the structure deduced by Reflection Adsorption Infrared Spectroscopy

(RAIRS)) in 12-18 hours, but there are evidences suggesting that the achievement of maximum packing density and minimum pinhole defects and conformational defects requires a slow reorganization process, sometimes taking ~7-10 days.⁽⁶⁸⁻⁷²⁾ The well ordered and densely packed SAMs are relatively stable in both air and vacuum for days to weeks.⁽⁶⁹⁾ Several research groups have reported that shorter chain length alkanethiolate SAMs (≤ 8) are more disordered and liquid-like than the longer chain length films.⁽⁶⁹⁻⁷²⁾ This is attributed to the decreased Van der Waals interactions between neighboring molecules.

In order to form thiolate SAMs, the thiol S-H bond needs to be broken. Hydrogen from the S-H group is lost either in the form of dihydrogen through the reductive elimination of H₂ from Au, or in the form of water through O₂ oxidation.⁽⁶⁸⁾ The formed Au-S bond is relatively strong and the bond strength is on the range of 50 kcal/mol.⁽⁶⁸⁾

The commensurate alkanethiol overlayer on Au (111) lattice is reported to adopt two structures, the $(\sqrt{3} \times \sqrt{3}) R30^\circ$ ^(73,74) structure and the $c(4 \times 2)$ superlattice.^(75,76) Figure 1.5 is a schematic diagram depicting these two arrangements with maximum surface coverage. The figure was adopted from reference 77. The alkanethiolate SAMs have a lattice spacing of $\sim 5 \text{ \AA}$ and a tilt angle of $\sim 35^\circ$ (relative to surface normal).^(68,78) As a comparison, SAMs composed of a mostly fluorinated hydrocarbon backbone adopt $p(2 \times 2)$ or $c(7 \times 7)$ structures with a lattice spacing of $\sim 5.9 \text{ \AA}$ and a tilt angle of $\sim 16^\circ$.⁽⁷⁸⁾ For the same substrate, the packing density is mainly determined by the nature of the chain backbone instead of the chemical structure of the terminal group. The halogenated

alkanethiolate self-assembled monolayers on gold used in this thesis will be listed in Chapter 2.

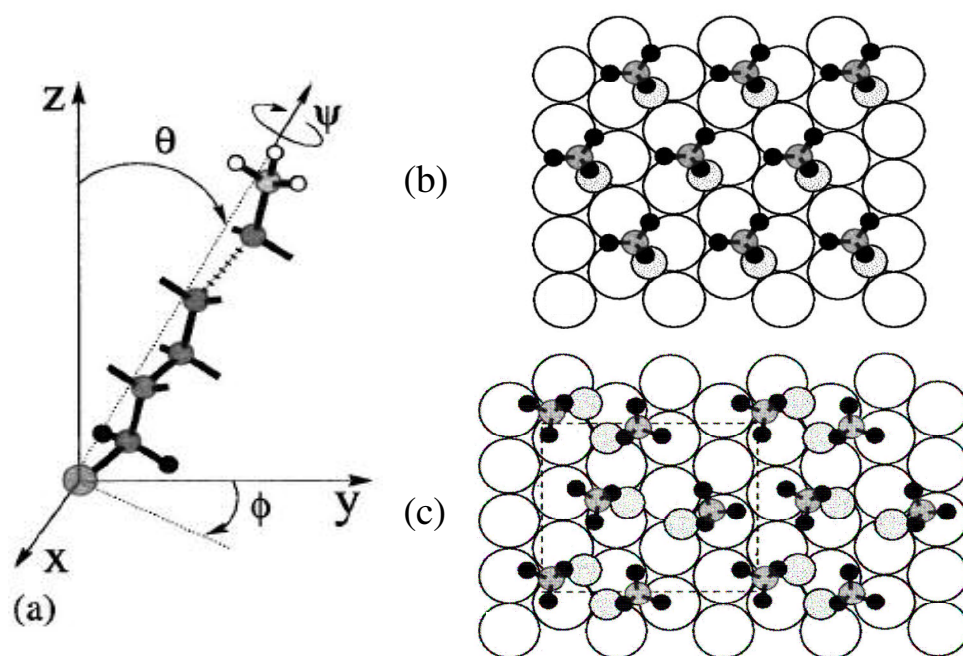
1.3 Questions to be addressed in this thesis

As mentioned in section 1.1.3, there remains much to be understood about the important processes that occur during ion-surface collision, such as conversion of a projectile ion's kinetic energy into internal energy, electron transfer through the SAM films and ion-surface reaction.

In Chapter 3, a series of halogen terminated alkanthiolate SAM films with gradually changing terminal mass and surface rigidity will be used to investigate which is the dominant factor that affects the energy transfer process. Also, total ion currents measured from the MS/MS instrument will be related to the surfaces' ionization energies and interface dipoles to determine which factor correlates better with the electron transfer and ion neutralization process. The ion-surface reactions of different SAM films with benzene, pyrazine, $W(CO)_6$, and CD_3^+ ions will also be examined.

Chapter 4 describes experiments in which the peptide YGGFLR was successfully soft-landed, *i.e.*, deposited, on three different surfaces. This is a start for the separation and collection of materials-chemistry related compounds as well as fragment ion structures that are of special interest in peptide and protein fragmentation.

Figure 1.5. Structural model of the *n*-alkanethiolate adlayer on gold lattice. (a) An alkanethiol molecule with a tilt angle of θ relative to the surface normal and a rotational angle ψ along the molecular axis. (b) is a $(\sqrt{3} \times \sqrt{3})R30^\circ$ structure where the sulfur atoms (light gray circles) are positioned in the 3-fold hollows of gold lattice (white circles, $a = 2.88 \text{ \AA}$). (c) is a $c(4 \times 2)$ superlattice structure marked by dashed line. The molecular S–C axis, is strongly tilted (45° – 53°) and hydrogen atoms are twisted with respect to those in the other molecule. Figure was adapted from reference 77. Reprinted with permission from **Structure and Energetics of Alkanethiol Adsorption on the Au (111) Surface**, by Yashar Yourdshahyan, Andrew M. Rappe. Copyright 2005, American Institute of Physics.



Chapter 2. Instrumentation and Experimental Methods

2.1 Instrumentation

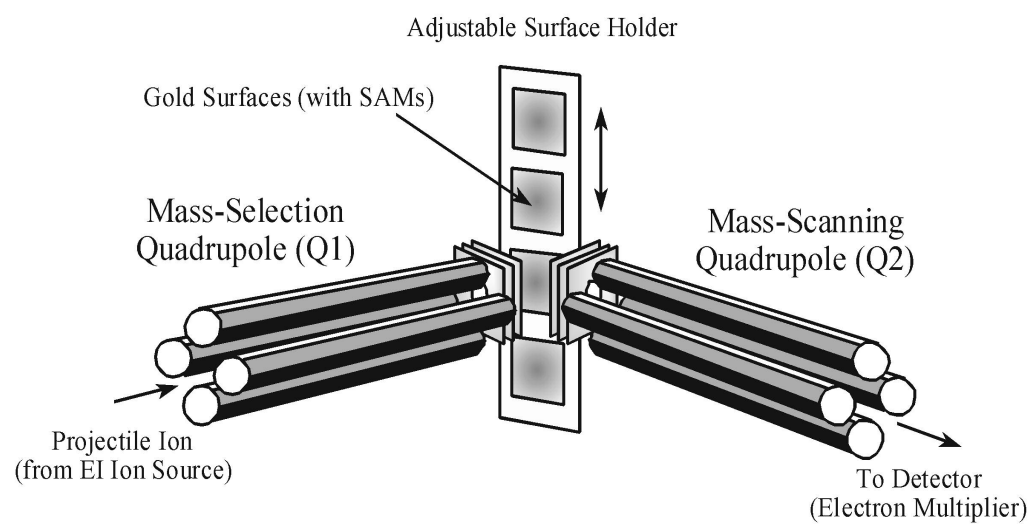
This chapter describes the instrumentations used in both Chapter 3 and Chapter 4, the thiol synthesis as well as preparation of SAM films. Most experiments were performed in a tandem mass spectrometer. Other instruments, including contact angle, XPS, and FT-IR, were also used to provide additional information for SAM films.

2.1.1 Dual-quadrupole SID mass spectrometer

All the low energy ion-surface collision experiments were performed on dual-quadrupole SID mass spectrometers. Two tandem mass spectrometers were used, an Extrel 2000 amu system for polyatomic ions and an Extrel 4000 amu for peptides. The schematics for the two mass spectrometers are basically the same except that the Extrel 2000 amu instrument allows mass detection up to 2000 amu and the Extrel 4000 amu instrument allows mass detection up to 4000 amu. Ions entering the Extrel 2000 amu instrument were produced by 70 eV electron impact ionization (EI). Standard operating parameters include a base pressure of 7×10^{-7} torr and sample pressure of 1×10^{-6} torr for small organic molecules, 2×10^{-6} torr for $W(CO)_6$ and deuterated acetone molecules. Ions entering the Extrel 4000 amu instrument were formed by electrospray ionization (ESI). Base pressure was around 6.8×10^{-7} torr and operating pressure was around 2.8×10^{-6} torr. Experimental details for the use of this instrument for soft landing are given in chapter 4.

Figure 2.1 shows the design of the dual-quadrupole SID tandem mass spectrometer. The figure adapted from reference 79. Two Extrel quadrupole analyzers are

Figure 2.1 Dual quadrupole SID tandem mass spectrometer. Figure adapted from reference 79.



arranged in a 90° geometry with a solid surface placed to intersect the ion optical path. The surface was positioned at an approximately 45° angle relative to the ion beam from the first quadrupole, Q1. Ions were mass selected by Q1 and allowed to collide into the surface at a desired collision energy. The collision energy was determined by the voltage difference between the source and the surface and can be systematically changed. To transmit ions past the surface without colliding them on the surface, the voltage difference was held at 0 eV. The collision products were analyzed by the second quadrupole and detected by a conversion dynode-electron multiplier assembly. The surface holder in the Extrel 2000 system is able to hold four surfaces at the same time and moves vertically to position four surfaces successively into the ion beam, which allows ion collisions on all the surfaces to be performed with the same tuning parameters and instrument conditions. The surfaces are connected in series by a metal plate at the back of the holder, and a single power supply is used to apply the same voltages to each of the surfaces.

2.1.2 Ultraviolet Photoemission Spectroscopy (UPS)

The XPS and UPS data were provided by Amy Graham, Dana Alloway, Paul Lee, and Kenneth Nebesny at University of Arizona. XPS and UPS were used to determine the chemical composition of the SAMs, as well as the ionization energy and vacuum-surface interface dipole of the surfaces. The difference between these two techniques is the energy of photon source used to generate photoelectrons. XPS was first developed by Siegbahn in the mid 1960s which won him the Nobel Prize for Physics in 1981. Photoemission spectroscopy is based on the photoelectric effect outlined by Einstein in

1905. When a photon with energy $h\nu$ impinges on a surface, this energy can be absorbed. If this energy is high enough, electrons can be ejected from the surface with their kinetic energy (E_k) defined by

$$E_k = h\nu - E_b - w \quad (\text{Eq. 2.1})$$

where E_b is the electron's binding energy and w is the work function of the instrument.⁽⁸⁰⁾

Figure 2.2 is a schematic representation of the physical process in XPS. For XPS, Al $K\alpha$ (1486.6 eV) or Mg $K\alpha$ (1253.6 eV) are the main choices for photon sources. The XPS data obtained in this thesis employed Al $K\alpha$ x -rays. When such high energy photons are used, electrons from inner shells K or L are ejected. The binding energy of the escaping electrons are characteristic of the atom and orbital from which the electrons were emitted. The photoelectron peak area is related to the amount of the material on the surface and can quantitatively determine the composition of surface materials with appropriate sensitivity factors.⁽⁸¹⁾ XPS can detect all the elements except hydrogen and helium. UPS adopts ultraviolet light as the photon source, usually a helium lamp emitting at 21.2 eV (He I radiation) or 40.8 eV (He II radiation). The UPS data (interface dipole and IE of the SAM films) obtained in this research used He I light. Compared to XPS, the photon energy is much lower, which means that only electrons from the valence band or shallow core levels can be ejected.

The X-ray photoelectron spectrometer instrument that provides the data presented in this thesis was a *Kratos* Ultra photoelectron spectrometer. Figure 2.3 shows the

Figure 2.2 Schematic representation of the XPS. Figure was modified from reference 80.

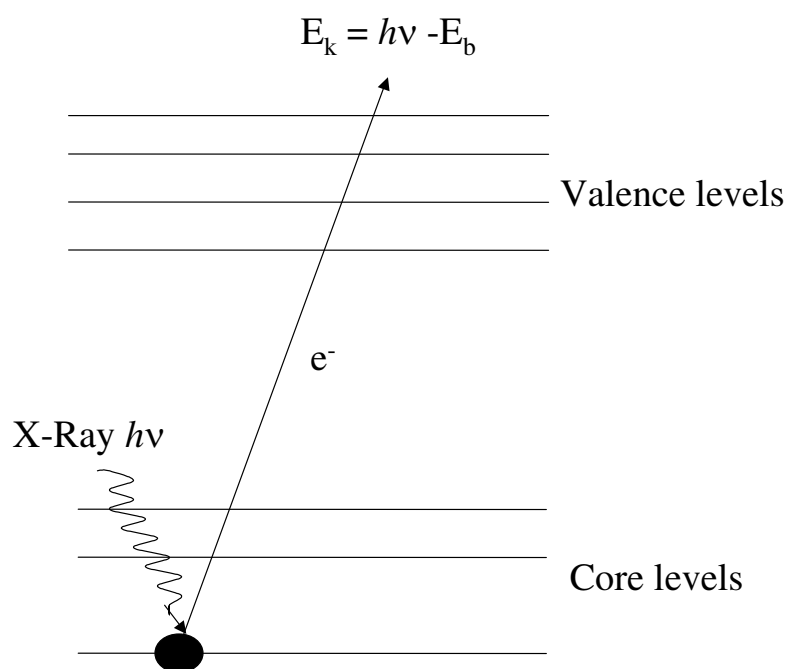
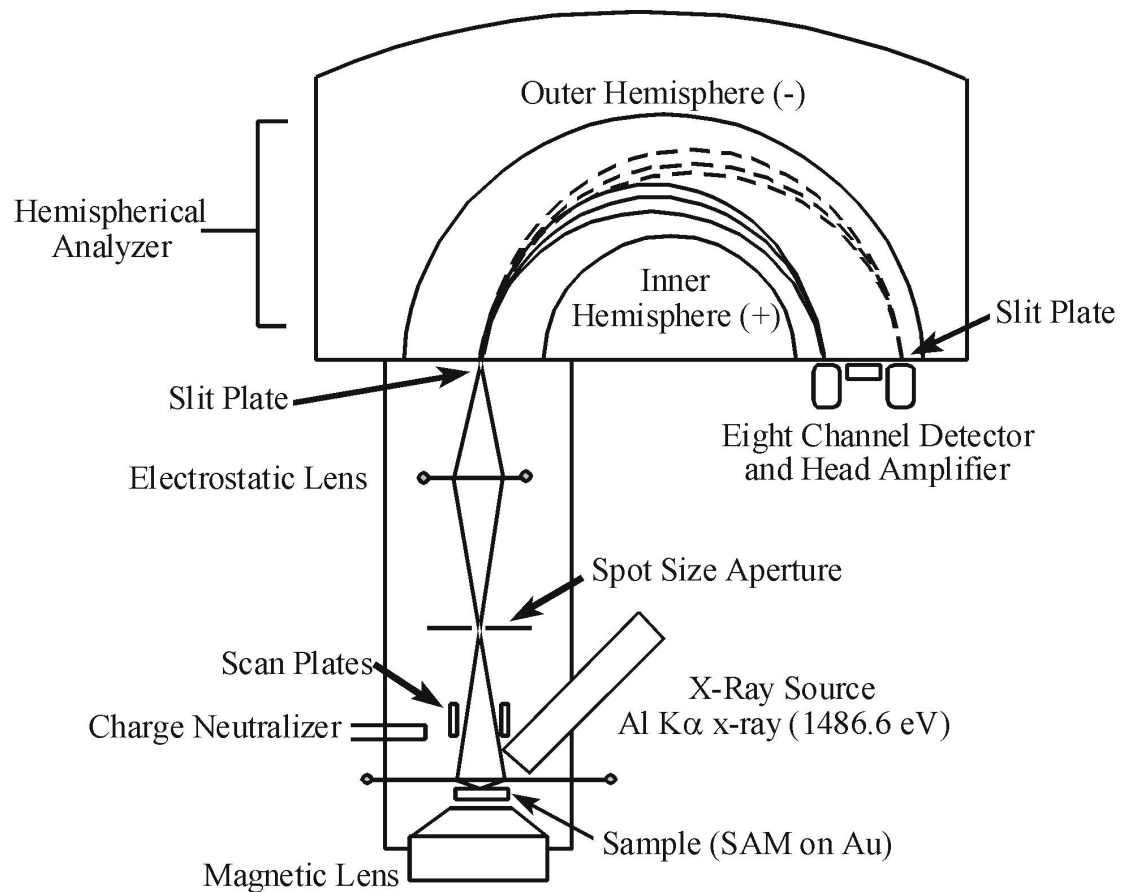


Figure 2.3 schematic of the *Kratos Ultra* photoelectron spectrometer. Figure modified from reference 77.



schematic of the *Kratos* Ultra photoelectron spectrometer.⁽⁸²⁾ The figure was modified from the *Kratos* website. The analysis area for this instrument is $\sim 700 \times 700 \mu\text{m}$. The energy of the ejected photoelectrons is determined by a concentric hemispherical analyzer. Electronic lenses are placed before the analyzer to focus photoelectrons into it and slow down the electrons to constant kinetic energy. The analyzer is composed of two hemispheres with different radii. Different voltages are applied to the two hemispheres, specifically, the outer one is negatively charged and the inner one is positively charged. An electric field is thus formed. Only photoelectrons from a narrow energy window (the pass energy) can pass through the analyzer and reach the detector. Photoelectrons with higher kinetic energy will collide with the outer hemisphere. Those with lower kinetic energy will collide with the inner hemisphere. For all UPS analysis, a 5 V bias was applied to improve the transmission of low E_k electrons and to improve the determination of the low- E_k edge. Separate UPS and XPS spectra were measured for a sputtered clean gold foil everyday before the measurement of SAM films to make sure that the instrument parameters were the same for all the experiments.

Gas-phase UPS spectra were provided by Dr. Nadine Gruhn at Center for Gas-phase Electron Spectroscopy, Department of Chemistry, University of Arizona. Gas-phase UPS data were obtained by an instrument that contains a 36-cm hemispherical analyzer (McPherson) and custom designed sample cells and detection and control electronics.⁽⁸³⁾ The excitation source was a quartz lamp with the ability to produce He I (21.21 eV) or He II (40.8 eV) photons. The ionization energy scale was calibrated by using the $^2E_{1/2}$ ionization of methyl iodide (9.538 eV), with the argon $^2P_{3/2}$ ionization

(15.759 eV) used as an internal energy scale lock during data collection. The alkanethiol C12 is a liquid and was introduced into the spectrometer from an internal aluminum sample cell that has been cooled to 10 – 18 °C. All other samples are solids and the data was collected with the samples in the aluminum sample cell heated to 35-40 °C. During data collection the instrument resolution was 0.020-0.030 eV measured using the full width at half-maximum of the argon $^2P_{3/2}$ ionization. All data are intensity corrected with an experimentally determined instrument analyzer sensitivity function that assumes a linear dependence of analyzer transmission (intensity) on the kinetic energy of the electrons within the energy range of these experiments.

2.1.3 Fourier transform Infrared spectroscopy (FT-IR)

Infrared (IR) radiation is electromagnetic radiation that encompasses all the wavelengths between the visible and microwave regions of the electromagnetic spectrum. The IR region can also be subdivided into three smaller regions known as near-IR, mid-IR and far-IR. Mid-infrared ($670 - 4000 \text{ cm}^{-1}$) absorption and reflection spectrometry are major tools for determining the structure of organic and biochemical species.⁽⁸⁰⁾ Only molecules that undergo a dipole change upon absorbing Infrared radiation are IR active. The strength of the dipole moment is determined by the magnitude of the charge difference and the distance between the centers of charge and as the molecule bends and stretches, the changing dipole moment establishes an electric field. When the alternating electric field of the electromagnetic radiation matches the molecule's vibrational frequency, interaction between the two fields may occur, resulting in resonant energy transfer and the amplitude change of the molecular vibration.

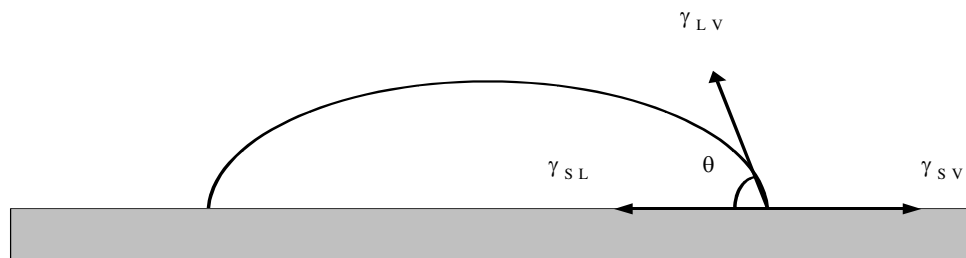
The IR technique used to probe SAM films in the current research is Reflection Adsorption Infrared Spectroscopy (RAIRS). For molecules sitting on a surface while vibrating, an infrared spectrum of light reflected from the surface will show absorption peaks which are characteristic of the molecules and their method of bonding to the surface as well as their orientation at metal surfaces. This is the basis of the RAIRS technique. Vibrations can only be detected if the vibration is perpendicular to the surface. Detection of the infrared spectrum is generally acquired using the FT-IR technique.

The instrument used to obtain RAIRS spectra in this thesis was a Nicolet 4700 Fourier transform infrared spectrometer equipped with a VeeMax II variable angle splitter reflectance accessory and a liquid nitrogen cooled narrow band MCT-A detector in Dr. Mary Wirth laboratory. The grazing angle used was 60° . A freshly cleaned gold surface was used as the background for all spectra. The spectrometer was set to collect 1000 scans at a spectral resolution of 4 cm^{-1} .

2.1.4 Contact angle

Contact angle is a quantitative measure of the wetting of a solid by a liquid. It is defined geometrically as the angle formed by a liquid at the three-phase boundary where a liquid, gas and solid intersect.⁽⁸⁴⁾ Figure 2.4 shows the schematic depiction of a drop of liquid on a solid surface. When the contact angle θ is lower than 90° , the liquid is considered to wet the solid. If it's greater than 90° , it is considered to be non-wetting. A zero contact angle means complete wetting. If the three phase (liquid-solid-vapor) boundaries are in actual motion, the angles are called Dynamic Contact Angles and are referred to as "advancing" and "receding" contact angles. The relationship between the

Figure 2.4 Depiction of a drop of liquid on a hydrophilic surface. γ_{SV} represents the free energy of the solid-vapor interface, γ_{LV} represents the free energy of the liquid-vapor interface, and γ_{SL} represents the free energy of the solid-liquid interface.



contact angle (θ), the free energy of the solid-vapor interface (γ_{SV}), the free energy of the liquid-vapor interface (γ_{LV}), and the free energy of the solid-liquid interface (γ_{SL}) is described by Young's equation⁽⁸⁵⁾:

$$\gamma_{LV}\cos\theta = \gamma_{SV} - \gamma_{SL} \quad (\text{Eq. 2.2})$$

Contact angle measurement has been shown to be sensitive to the chemical composition and physical structure of the outermost few angstroms of organic thin films.⁽⁷⁶⁾ Both polar and nonpolar contacting liquid have been used.⁽⁸⁵⁻⁸⁷⁾ Water and hexadecane are the two most often used liquids. Water has a high surface tension due to its polarity and ability to form hydrogen bonds. It provides information on the polarity changes at the surface-liquid interface. In contrast, hexadecane has lower surface tension and gives information on the nonpolar changes of the interface.⁽⁸⁷⁾ In this research, advancing contact angles for various surfaces were measured at 295 K and ambient relative humidity using Krüss DSA10 contact angle measuring instrument. The contacting liquid was Millipore water (18.0 M Ω). A 2.0 μl drop was initially placed on the surface and the drop is increased with increments of 0.25 μl with the needle remaining in the drop (drops added with rate 50 $\mu\text{l}/\text{min}$). A camera snapshots the image and the contact angle was measured using method Tangent 1. The data were collected and averaged over three separate slide using 5 spots per slides for each type of surface.

2.2 Organic thin films on Au substrate

A number of thiolate SAM films were used in the studies presented in this thesis. The thiols were obtained from different sources. Some of them are commercially available (see below) and some of them had to be synthesized.

2.2.1 Synthesis and listing of SAMs used in the thesis

Table 2.1 lists the alkanethiol compounds used to make self-assembled monolayers on gold. The table also lists the structure and abbreviation of these compounds. The *n*-alkanethiol C12 (98%) was purchased from Aldrich and used without further purification. C11 was kindly provided by Dr. Lee's group from the University of Houston, TX. The C11NH₂ (94.6%) was purchased from Dojindo, Japan and used without further purification. The C11OH and C12F10 thiols were synthesized and purified from the corresponding alkyl bromide or iodide (HO(CH₂)₁₁Br, 99%, purchased from Sigma; CF₃(CF₂)₉(CH₂)₂I, 98%, purchased from SynQuest Laboratories, Inc. FL) as previously described.⁽⁸⁸⁾C14F1 is an appreciated gift from Dr. Lee's group from the University of Houston, TX. The synthesis of C12Cl and C12Br is described below. All the synthesis was performed by Ron Wysocki in the Chemical Synthesis Laboratory at the University of Arizona. General. All reactions were performed under a nitrogen atmosphere. All commercially available materials were used as is without further purification. Thiobenzoic acid (90+ %) and 1,12-dibromododecane were purchased from TCI America. Sodium hydride (NaH, 60 % dispersion in mineral oil) was obtained from Aldrich. *N,N*-Dimethylformamide Photrex[®] Reagent grade was obtained from JT Baker. Diethyl ether, ethyl acetate, hexanes and pentane were obtained from EMD Chemicals. Ethanol (USP, 200 Proof) was obtained from Aaper Alcohol and Chemical. Thin Layer Chromatography (TLC) was performed on Analtech glass-backed silica gel GF Uniplates[®] Visualization was performed by ultraviolet detection or exposure of plate to

Table 2.1 Thiol compounds and abbreviations for SAM films used in this research.

Thiol compounds	Abbreviation	Source
$\text{CF}_3(\text{CF}_2)_9(\text{CH}_2)_2\text{SH}$	C12F10	Synthesis
$\text{CF}_3(\text{CH}_2)_{13}\text{SH}$	C14F1	Dr. Randall Lee, University of Houston
$\text{Cl}(\text{CH}_2)_{12}\text{SH}$	C12Cl	synthesis
$\text{Br}(\text{CH}_2)_{12}\text{SH}$	C12Br	synthesis
$\text{CH}_3(\text{CH}_2)_{11}\text{SH}$	C12	Aldrich
$\text{CH}_3(\text{CH}_2)_{10}\text{SH}$	C11	Dr. Randall Lee, University of Houston
$\text{HO}(\text{CH}_2)_{11}\text{SH}$	C11OH	synthesis
$\text{NH}_2(\text{CH}_2)_{11}\text{SH}$	C11NH ₂	Dojindo, Japanese

iodine (I_2) vapor. Flash Chromatography¹ was performed on Geduran[®] Silica Gel 60 (SiO_2 , 35-70 μm) obtained from EMD Chemicals. Deuteriochloroform (CDCl_3) was obtained from Cambridge Isotope Laboratories. Nuclear magnetic resonance spectra (NMR) were obtained on a Varian Unity 300 MHz instrument. Fast Atom Bombardment Mass Spectra (FABMS) were obtained on a JEOL HX 110 EB Sector instrument in a matrix of 50 % glycerol, 25 % thioglycerol and 25 % *m*-nitrobenzyl alcohol. Gas Chromatography Mass Spectra (GCMS) were obtained on a Varian Saturn 2000 instrument.

Thiobenzoic acid, S-(12 bromo-1-dodecyl) ester. A 250 mL round bottom flask

equipped with a Teflon[®] coated magnetic stir bar was charged with DMF (20 mL) and 1,12-dibromododecane (6.13 g, 18.7 mmol) was cooled in an ice bath. A pressure equalized addition funnel was attached and the reaction solution was allowed to stir. Sodium thiobenzoate was prepared as follows: a suspension of sodium hydride (970 mg, 24.2 mmol) was washed with hexanes (3 x 8 mL). The dry powder was suspended in DMF (20 mL). Thiobenzoic acid (2.0 mL, 16.5 mmol) was added dropwise via syringe to the sodium hydride DMF reaction mixture over 0.25 h at room temp. After bubbling stopped, the freshly generated sodium thiobenzoate DMF mixture was transferred to the pressure-equalized addition funnel.

The sodium thiobenzoate mixture was added dropwise to the cold 1,12-dibromododecane DMF solution. Once addition was complete, the ice bath was removed and the reaction mixture was stirred at room temperature overnight. After 20 h, the reaction mixture was diluted with ether (50 mL) and was treated with ice water dropwise until bubbling ceased. The mixture was then diluted with water (20 mL) and extracted with ether (2 x 100 mL). The ether extracts were combined, washed with water (1 x 100 mL), sat. aq. NaCl (1 x 100 mL), dried (MgSO₄) and concentrated in vacuo. Flash chromatography (SiO₂, 3.5 cm x 15 cm, hexanes eluent) afforded in order of elution: recovered 1,12-dibromododecane (R_f 0.50); the desired product (2.5 g, 6.36 g theoret., 39 %); and the by product thiobenzoic acid, *S,S'*-1,12-dodecanediyl ester (1.3 g).

Thiobenzoic acid, *S*-(12 bromo-1-dodecyl) ester. TLC data (R_f 0.38, hexanes); ¹H NMR (CDCl₃, 300 MHz) δ : 7.97 (d, 2 H, J = 8.0 Hz, ortho aromatic H), 7.60-7.40 (m, 3 H, para and meta aromatic H), 3.4 (t, 2 H, J = 7.5 Hz, CH₂Br), 3.1 (t, 2 H, J = 7.5 Hz,

$CH_2SC=O$), 1.85 (quintet, 2H, $J = 7.5$ Hz, CH_2CH_2Br), 1.65 (quintet, 2 H, $J = 7.5$ Hz, $CH_2CH_2SC=O$), 1.50-1.22 (m, 16H, CH_2); FABMS (m/z, relative abundance): 385 (49, $C_{19}H_{29}^{79}BrO^{32}S + H^+$), 387 (51, $C_{19}H_{29}^{81}BrO^{32}S + H^+$ and $C_{19}H_{29}^{79}BrO^{34}S + H^+$).

Thiobenzoic acid, *S,S'*-1,12-dodecanediyl ester. TLC data (R_f 0.2, hexanes); 1H NMR (300 MHz, $CDCl_3$) δ : 8.01 (d, 4 H, $J = 8.0$ Hz, ortho aromatic H), 7.60-7.40 (m, 6 H, meta and para aromatic H), 3.09 (t, 4 H, $J = 7.4$ Hz, SCH_2), 1.78-1.20 (m, 20 H, $SCH_2(CH_2)_{10}CH_2S$).

12-Chloro-1-dodecanethiol. A mixture of thiobenzoic acid, *S*-(12-bromo-1-dodecyl) ester (697 mg, 1.81 mmol) in ethanol (8 mL) was treated with concentrated aqueous HCl (1 mL). The reaction mixture was sealed in a glass tube equipped with a threaded Teflon® plug. The reaction mixture was placed into a hot oil bath and was stirred. After 48 h, the reaction mixture was cooled to room temperature and was extracted with pentane (3 x 20 mL). The pentane layers were combined, washed with ice water (4 x 20 mL), dried ($MgSO_4$) and concentrated in vacuo. Flash chromatography (SiO_2 , 3.5 cm x 15 cm, 2 % ethyl acetate-hexanes eluent) afforded 12-chloro-1-dodecanethiol (115 mg, 429 mg theore., 27 %) as a colorless oil. TLC data (R_f 0.75, 4 % ethyl acetate in hexanes); 1H NMR (300 MHz, $CDCl_3$) δ : 3.54 (t, 2H, $J = 7.4$ Hz, $ClCH_2$), 2.51 (quartet, 2H, $J = 7.4$ Hz, CH_2CH_2SH), 1.76 (quintet, 2H, $J = 7.4$ Hz, $ClCH_2CH_2$), 1.61 (quintet, 2H, $J = 7.4$ Hz, CH_2CH_2SH), 1.49-1.20 (m, 17H, $ClCH_2CH_2(CH_2)_8CH_2CH_2SH$); GCMS m/z 237 ($C_{12}H_{25}^{37}ClS^+$), 235 ($C_{12}H_{25}^{35}ClS^+$), 200 (base, $M^+ - Cl$).

12-Bromo-1-dodecanethiol. A mixture of thiobenzoic acid, *S*-(12-bromo-1-dodecyl) ester (970 mg, 2.52 mmol) in ethanol (20 mL) was treated with concentrated aqueous HBr (48 %, 10 mL) and concentrated sulfuric acid (H₂SO₄, 1 mL). The reaction mixture was sealed in a glass tube equipped with a threaded Teflon® plug. The reaction mixture was placed into a hot oil bath (100 °C) and was stirred. After 72 h, the reaction mixture was cooled to room temperature and was extracted with pentane (3 x 20 mL). The pentane layers were combined, washed with ice water (4 x 20 mL), dried (MgSO₄) and concentrated in vacuo. Flash chromatography (SiO₂, 2.5 cm x 15 cm, 2 % ethyl acetate-hexanes eluent) afforded 12-bromo-1-dodecanethiol (139 mg, 708 mg theoreti., 20 %) as a colorless oil. TLC data (R_f 0.75, 4 % ethyl acetate in hexanes); ¹H NMR (300 MHz, CDCl₃) δ: 3.39 (t, 2H, *J* = 7.4 Hz, BrCH₂), 2.51 (quartet, 2H, *J* = 7.4 Hz, CH₂CH₂SH), 1.84 (quintet, 2H, *J* = 7.4 Hz, BrCH₂CH₂), 1.58 (quintet, 2H, *J* = 7.4 Hz, CH₂CH₂SH), 1.49-1.25 (m, 17H, BrCH₂CH₂(CH₂)₈CH₂CH₂SH); GCMS *m/z* 281 (MH⁺), 201 (MH⁺ - HBr)

2.2.2 Preparation of SAM surfaces

The vapor-deposited gold surfaces were purchased from Evaporated Metal Films (Ithaca, NY). The gold surfaces were formed on a 17 mm × 13 mm × 0.5 mm silica base that was covered with a 5 nm adhesion underlayer of titanium and then 100 nm of evaporated gold. Roughness of gold is about 1 - 2 nm. The gold surfaces were UV-Ozone cleaned for 15 minutes (Boekel UV cleaner, model 135500, Boekel Industries, Inc. PA) before being placed in appropriate thiol solutions. Solutions of various thiols (~1 mM) were prepared in glass volumetric flasks that were pre-cleaned with piranha solution

($\text{H}_2\text{SO}_4/\text{H}_2\text{O}_2$ in a 1:3 volume ratio) for 1 hr. *Caution: piranha solution reacts violently with organic materials and should be handled with extreme care!* Then 5 mL aliquots of each thiol solution were transferred to disposable test tubes that were rinsed with ethanol and UV-cleaned for 5 min. The fresh cleaned gold surfaces were placed in thiol solutions and allowed to react for 72 hr for single component SAM and 24 hr for mixed SAM. The films were then rinsed six times by sonication in ethanol, dried under nitrogen, and inserted into the mass spectrometer within 5 minutes.

Chapter 3. Ion Surface Collision as a Tool for Probing both Projectile Ions and Halogen Terminated SAM Films

3.1 Introduction

Ion-surface collision has been of interest for the past two decades due to its applications in surface modification^(89,90) and tandem mass spectrometry.^(40,51,91,92) In tandem mass spectrometry, ion-surface collision is an alternative ion activation method to collision-induced dissociation (CID) and has been used for atomic and small molecular ions^(42,43,93,95) as well as large biomolecules.^(13,14,34,50) Compared to CID, SID converts more of the projectile ions' kinetic energy into their internal energy.^(31,32) Although it is generally believed that SID provides a more narrow internal energy distribution than CID,^(31,32) recent studies by Laskin *et al.* demonstrated that SID and multiple collision CID have similar internal energy distributions.⁽²⁰⁾ Surfaces commonly used in these experiments include self-assembled monolayers (SAMs) of n-alkanethiols (HSAMs) and their partially fluorinated analogs (FSAMs). Previous studies have shown that FSAMs and HSAMs are well ordered surfaces, and films with similar backbones have similar packing densities⁽⁷⁸⁾ on the same substrate. Studies of collisions of ions with surfaces can either make use of SAM films as standard targets to study projectile ion fragmentation^(8,47) or use well studied ion beams to probe SAM films as model surfaces.^(42,96,97)

One important process that occurs during ion-surface collision is the conversion of kinetic energy to internal energy (T→V) for the projectile ion. Although the chemical compositions of both the projectile ion⁽⁴⁰⁾ and the SAM surface affect the amount of internal energy deposited into the projectile ions, that of the surface is the main determinant.⁽⁴¹⁾ It has been shown that the kinetic to internal energy transfer for the projectile ion is more efficient on fluorinated surfaces than on hydrocarbon surfaces, which can be attributed to the increased effective mass of the terminal group^{(41,92,96 98} and also to the surface rigidity.⁽⁹⁹⁾ There have been different opinions on which one of the two factors dominates the energy deposition. Wysocki and coworkers investigated SID on both hydrocarbon and fluorocarbon surfaces⁽⁴¹⁾ and demonstrated that the energy deposited to the projectile ion is predominantly determined by the effective mass of the end group. Specifically, the T→V conversion was 18.8% on C16 (CH₃(CH₂)₁₅SH) SAM surface, 26.5% on C16F1 (CF₃(CH₂)₁₅SH) SAM surface and 28.2% on C16F10 (CF₃(CF₂)₉(CH₂)₆SH) SAM surface when using benzene as projectile ion. The fact that C16F10 surface converts more of the projectile ion's kinetic energy to its internal energy compared to C16F1 surface indicates that the underlying (CF₂)_n groups also play a measurable role. In other words, the (CF₂)_n backbone increases both the terminal mass and rigidity of C16F10 film. A quantitative study by Futrell and Laskin⁽⁹²⁾ made the same conclusion based on collisions of protonated peptide ions with diamond, LiF, HSAM and FSAM surfaces. The effective mass of HSAM and LiF surfaces are lower than that of diamond and FSAM surfaces, and the stiffness of the four surfaces increase in the order of HSAM < FSAM < LiF < diamond. They found that the percentage of T→V transfer

increases in the order of HSAM (10.1%), LiF (12.0%), diamond (19.2%), and FSAM (20.5%), which is in agreement with the order of the effective mass but not with that of the surface stiffness. Hase and Meroueh presented the opposite opinion.⁽⁹⁹⁾ They suggested that surface stiffness plays a major role in the energy transfer process. Their classical trajectory simulation study compared the $\text{Cr}(\text{CO})_6^+$ SID on diamond (111) and n-hexane thiolate SAM (HSAM)⁽⁹⁹⁾, and the results showed that the kinetic to internal energy transfer is 21% on “soft” HSAM and 56% on the “hard” or “stiff” diamond surface. Sagiv *et al.* proposed another theory which states that the energy transfer into projectile ion is dependent on the mass ratio of the projectile ion and the surface’s terminal group.⁽¹⁰⁰⁾ As this ratio approaches 1, the energy deposition is highest. For the same projectile ion, surfaces with higher terminal mass have higher internal energy deposition. Since this theory has the same idea as the first opinion proposed by Wysocki⁽⁴¹⁾ and Futrell⁽⁹⁾, they will be discussed together.

Neutralization is another important process that occurs during ion-surface collision. It occurs by electron transfer from the surface to the incoming projectile ion. SAMs have been shown to act as a barrier to this electron transfer process.⁽⁹¹⁾ The resultant amount of ion signal depends on the chemical composition of both projectile ion and SAM surface, and it has been shown that electron transfer and neutralization are more extensive on an HSAM than on an FSAM surface for a number of organic and inorganic polyatomic projectiles.^(41,42,45,46) The mechanism for electron transfer during SID is still under investigation. Currently there are two main theories proposed. First, the amount of neutralization at SAM surfaces is roughly dependent on the difference between

the ionization energy of the organic surface species and the recombination energy of the projectiles.^(41,42,45) Actually, it has been found that the higher ionization energy of the fluorinated versus the hydrocarbon surface accounts for the decreased neutralization of small organic projectile ions on fluorocarbon surfaces.^(41,45) Second, the surface/vacuum interface dipole may change the effective work function of the surface and thus influence electron transfer. UPS studies by Professor Neal Armstrong's group showed that a FSAM has a large negative interface dipole (pointing away from the gold substrate) which leads to a shift (increase) in the vacuum level compared to gold and thus increases the effective work function.⁽⁴⁶⁾ As a result, it's more difficult for the electrons to escape and for the incoming ions to be neutralized. On the other hand, HSAM has a large positive interface dipole (pointing toward the gold substrate) which lowers the effective work function and results in easier electron escape and more ion neutralization.

Ion-surface collisions also produce reaction products between the projectile ion and the target surfaces. Abstractions of C_nH_m and/or H from hydrocarbon surfaces and F from fluorocarbon surfaces has been observed.^(41,42,47) It has been reported that ion-surface reactions are sensitive to the chemical composition and orientation of the uppermost portion of the film.^(41,47,49,51) The sensitivity of ion-surface reactions to small changes in film orientation is illustrated in a study by Angelico *et al.*⁽⁵¹⁾ In this study, the relative abundances of reaction product ions were measured as a function of chain length for two classes of SAM films, *n*-alkanethiols ($CH_3(CH_2)_n-S-Au$, $n = 14-17$) and 4-(4-alkoxyphenyl)-benzenethiols ($4-(4-CH_3(CH_2)_mOC_6H_4)-C_6H_4-S-Au$, $m = 14-17$). SAMs with odd (n & $m = 14$ & 16) number chain length showed a consistently higher relative

abundance of H-addition product ions (measured as a percentage of the total ion current) compared with even chain length SAM films (n & $m = 15$ & 17). This result can be explained by the odd- versus even- orientation differences where odd-chain-length films are oriented with the last C-C bond more parallel to the plane of the surface than the even-chain-length films. It was hypothesized that the parallel orientation of the terminal C-C bond of odd-chain-length films presented the incoming ion with more accessible hydrogen atoms than the orientation adopted by the even-chain-lengths. Three mechanisms have been proposed to explain the ion-surface reactions. One states that the reaction is initiated by electron transfer between the ion and the surface which results in dissociation of the organic films and the ionized surface species then attach to the neutralized projectile.⁽⁹⁶⁾ Another mechanism is that the fragmentation of the surface species is induced by momentum transfer during the ion-surface collision. The work done by Morris *et. al.* supports the second possibility.⁽⁴²⁾ They observed that the threshold of ion-surface reaction products often roughly correlated with the threshold for SID. The third mechanism is a direct reaction mechanism (Eley-Rideal) where the incident ion reacts with the chemisorbed reagents without itself adsorbing on the surface.⁽¹⁰¹⁾ The study described here only tries to determine which ion-surface reactions happen on C12Cl and C12Br surfaces and is not designed to determine the reaction mechanism.

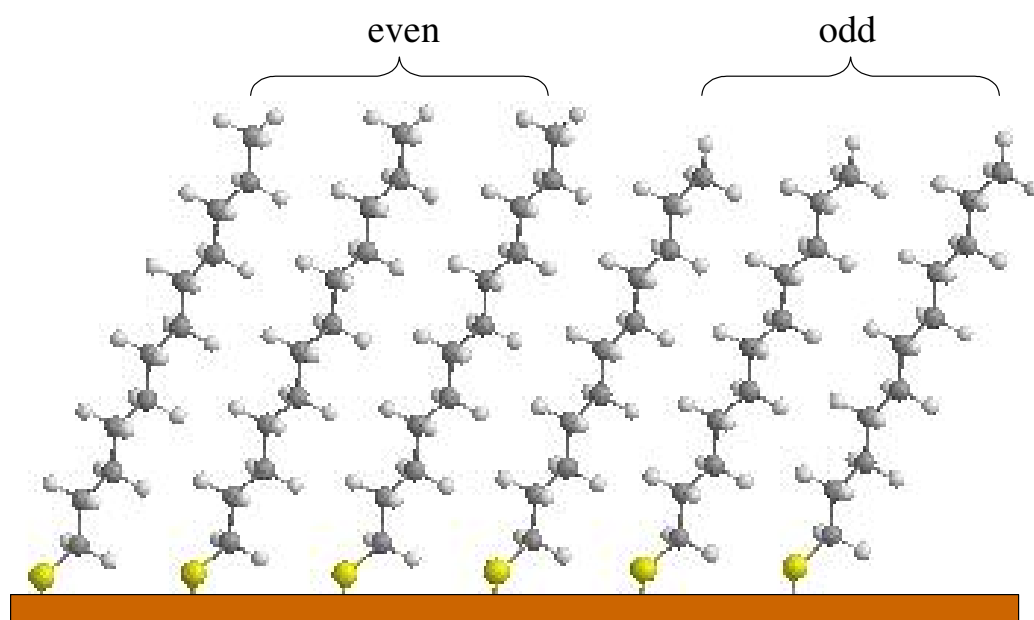
The present study compares the SID results obtained from a series of SAM films with different terminal groups, namely, C12F10 ($\text{CF}_3(\text{CF}_2)_9(\text{CH}_2)_2\text{SH}$), C14F1 ($\text{CF}_3(\text{CH}_2)_{13}\text{SH}$), C12Cl ($\text{Cl}(\text{CH}_2)_{12}\text{SH}$), C12Br ($\text{Br}(\text{CH}_2)_{12}\text{SH}$), and C12 ($\text{CH}_3(\text{CH}_2)_{11}\text{SH}$). Two CF₃-terminated surfaces were chosen for complementary study

since C12F ($\text{F}(\text{CH}_2)_{12}\text{SH}$) and C12F1 ($\text{CF}_3(\text{CH}_2)_{11}\text{SH}$) were not available. C14F1 has the same CH_2 backbone as other surfaces but is two methylene groups longer. C12F10 has the same chain length as other surfaces but its backbone is mostly fluorinated. The knowledge obtained in the current study will add to our fundamental understanding of ion-surface interactions. The specific questions to be answered by the research described here are: which is the dominant factor that determines the energy transfer to projectile ion, the terminal mass or surface rigidity? Do different projectile ions give same trend in energy transfer? Does surface IE or interface dipole mainly controls the neutralization of incoming ions? What ion-surface reactions occur on C12Cl and C12Br surfaces? Do these reactions include halide transfer that is parallel to the hydride and CH_3^- transfer that occur from CH_3 -terminated hydrocarbon SAM surfaces?

3.2 Results and discussion

According to previous studies⁽⁵¹⁾, SAMs with even number chain lengths have the terminal C-C bond more perpendicular to the substrate and the C-H bond more parallel to the surface. Figure 3.1 shows a ChemDraw 3D model for the comparison of odd (11 carbons as an example) and even (12 carbons as an example) number chain lengths of hydrocarbon surfaces. The tilt angle used was $\sim 30^\circ$ and the S-S distance was $\sim 5 \text{ \AA}$ which are close to the reported values.^(68,78) The Van der Waals radii and all trans packing were designated by ChemDraw. Due to the big Van der Waals radii of the Cl (0.99 \AA) atom and the Br (1.14 \AA) atom compared to that of the F (0.72 \AA) and the H (0.32 \AA) atoms, it's possible that C12Cl and C12Br surfaces would not pack as well as FSAM or HSAM

Figure 3.1. Comparison of even (left two chains, 12 carbons) and odd (right two chains, 11 carbons) chain lengths hydrocarbon SAMs. Figure was drawn by ChemDraw 3D.



because of the potential crowding of terminal groups. To determine whether this is true, ChemDraw 3D molecular models of CF_3 , CH_2Cl , CH_2Br , and CH_3 terminal groups are shown in Figure 3.2. It can be seen that Cl atom on the CH_2Cl group and Br atom on the CH_2Br group extend a little out of the terminal plane which relieves the crowding of the terminal groups and enables C12Cl and C12Br surfaces to have ordered packing. Reflection-absorption Fourier Transform infrared spectroscopy was also performed to provide insight into the packing (crystalline versus liquid-like) of the surfaces. Figure 3.3 shows FT-IR spectra in the $3050\text{-}2750\text{ cm}^{-1}$ region. The peaks at 2850 and 2919 cm^{-1} correspond to $\nu_s(\text{CH}_2)$ and $\nu_a(\text{CH}_2)$ stretching modes respectively (s = symmetric, a = asymmetric). The peak frequency for $\nu_s(\text{CH}_2)$ mode of an all-trans alkyl chain in an ordered crystalline environment is reported to be $2846\text{-}2850\text{ cm}^{-1}$, and that for the $\nu_a(\text{CH}_2)$ mode is reported to be $2915\text{-}2920\text{ cm}^{-1}$.^(70,102-104) For liquid-like disordered chains, the frequencies for the $\nu_s(\text{CH}_2)$ and $\nu_a(\text{CH}_2)$ modes increase to approximately 2856 and 2928 cm^{-1} , respectively.⁽¹⁰⁵⁾ Because the $\nu_s(\text{CH}_2)$ and $\nu_a(\text{CH}_2)$ peaks for all the surfaces fall within the ordered crystalline range, it suggests that the C14F1, C12Cl, C12Br and C12 surfaces produce well packed films.

The surfaces studied were also examined with the contact angle technique. Contact angle measurements have been shown to be sensitive to the chemical composition^(69,106) and phase separation which influence the interfacial wettability of the surface.^(84,107) The probing liquid used here is water which is sensitive to the polarity of the surface. The advancing contact angles (θ_a) measured with water on a series of surfaces are provided in Table 3.1.

Figure 3.2. Side view of idealized structure for C12F1 (CF_3 terminal group), C12Cl (CH_2Cl terminal group), C12Br (CH_2Br terminal group), and C12 (CH_3 terminal group) SAMs. Figure was drawn by ChemDraw 3D.

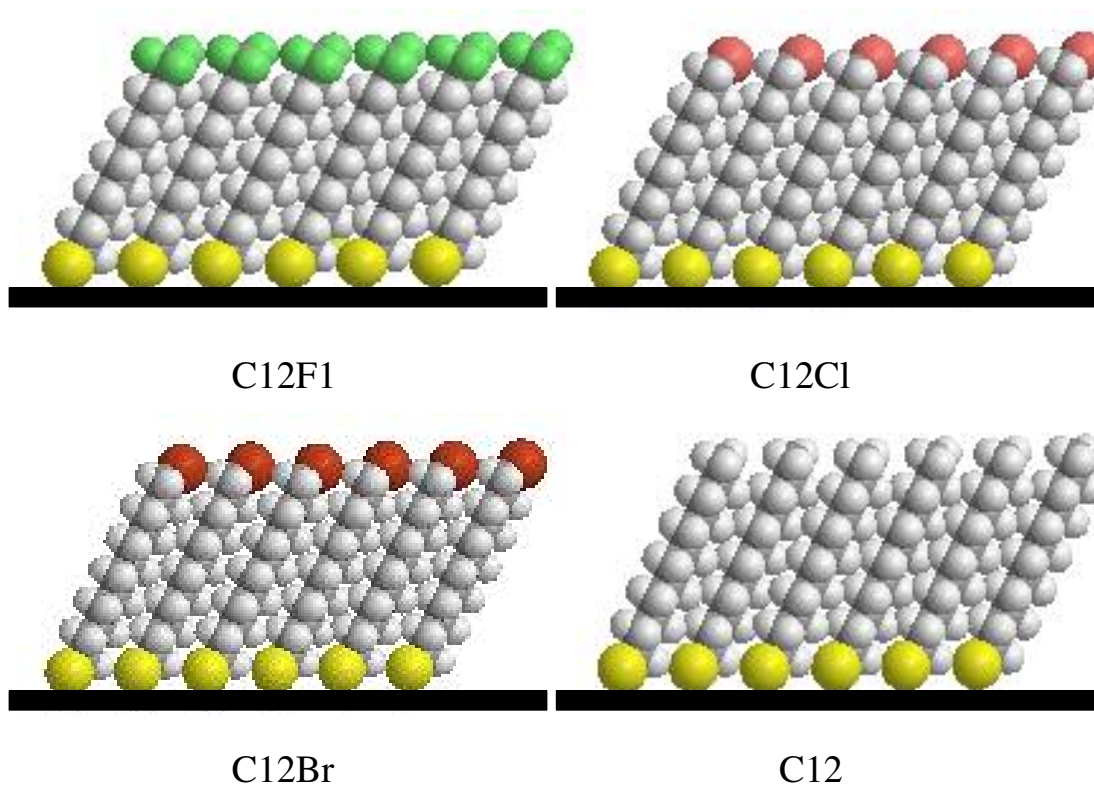


Figure 3.3. Methyl and methylene stretching region of the reflection absorption FT-IR spectra of C14F1, C12Cl, C12Br, and C12 surfaces.

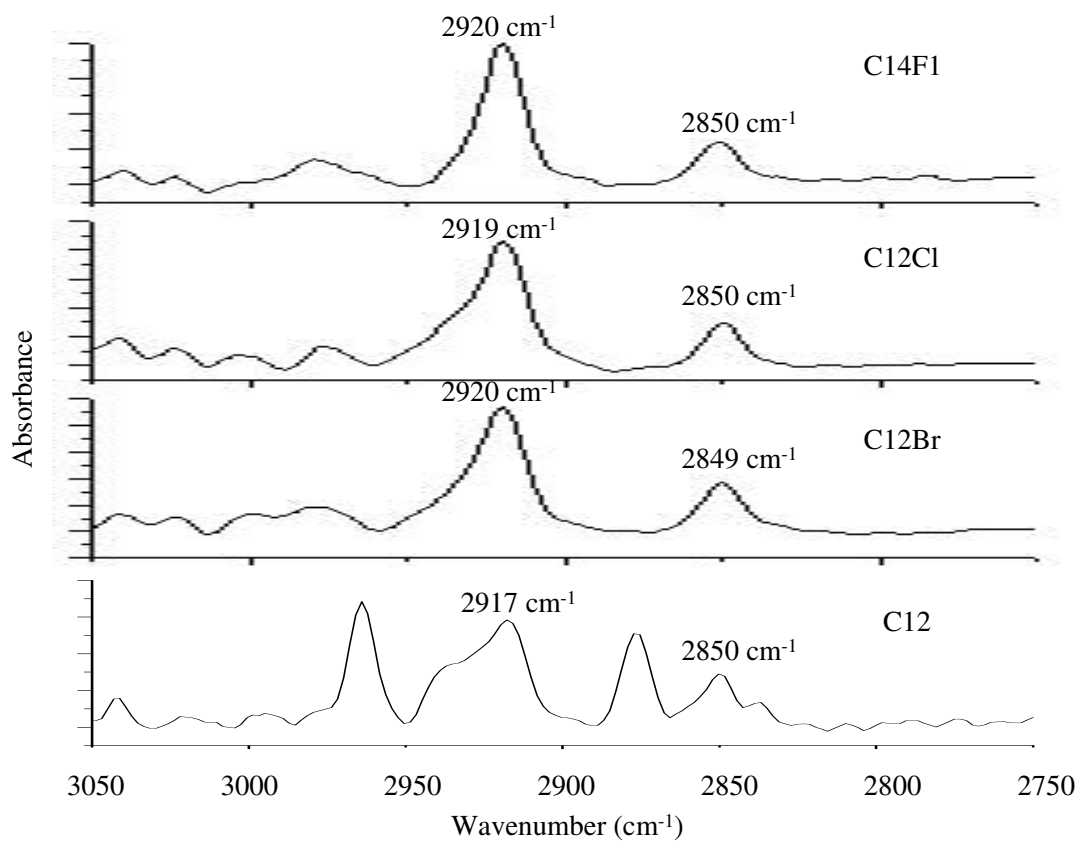
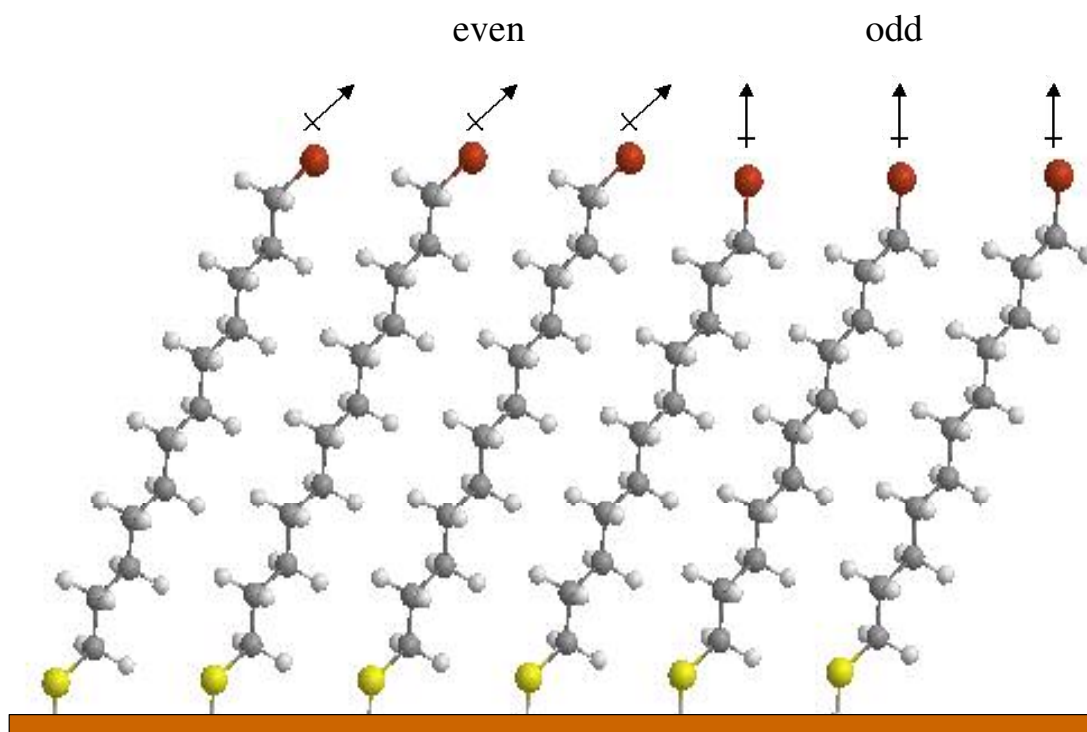


Table 3.1. Water advancing contact angle for C12F10, C14F1, C12Cl, C12Br, C12 surfaces.

Surface	C12F10	C14F1	C12Cl	C12Br	C12
Contact angle	124.4±2.1	105.0±0.8	87.9±2.1	87.4±1.6	113.0±2.7

The C14F1 surface wets more than the C12 surface due to attractive interactions between the permanent dipoles of H₂O and the oriented fluorine-hydrogen dipoles at C14F1 surface.⁽⁸⁵⁾ The contact angle for C12F10 increases about 20° compared to C14F1 surface because the fluorine-hydrogen dipole (determined by the location of the CF₂-CH₂ bond) is deeply buried beneath the monolayer surface.⁽⁸⁶⁾ Low contact angles for C12Cl and C12Br surfaces are due to the polarity of Cl and Br atoms which increases the interactions between the permanent dipoles of H₂O and the oriented CH₂Cl-CH and CH₂Br-CH dipoles. The contact angle data for C12F10 and C12 surfaces are consistent with the reported values,⁽¹⁸⁾ but that for C12Cl and C12Br surfaces are a little higher than the reported C11Br SAM (83°).⁽⁶⁹⁾ These differences might be due to the measurement error of the method itself or different orientation of the interface dipoles for C11Br and C12Br surfaces (odd-even effects). Specifically, the odd-number chain length C11Br surface have the interface dipoles nearly normal to the surface while the even-number chain length C12Br film presents at the surface an array of dipoles more tilted. Therefore, the interaction between water and the interface dipoles is stronger for odd-number chain length C11Br surface which results in enhanced wettability and lower contact angle. Figure 3.4 shows the odd-even effect of the surface dipoles.

Figure 3.4. Illustration of different dipole orientations of C12Br and C11Br surfaces.



3.2.1 Conversion of kinetic energy into internal energy for projectile ions

The spectra of benzene molecular ion (m/z 78) colliding with C14F1, C12Cl, C12Br, and C12 surfaces at 30 eV collision energy are given in Figure 3.5. Higher energy deposition is reflected by a decrease in the relative abundance of the precursor ion m/z 78 and an increase of the low mass fragments at m/z 26, 27, 39, 50-52, and 63. The spectra of pyrazine molecular ion (m/z 80) colliding on the same surfaces at 20 eV collision are given in Figure 3.6. Higher energy deposition is reflected by a decrease of the m/z 80 molecular ion and an increase of its fragments at m/z 26 and 53. Peaks that are related to ion-surface reactions such as m/z 91, 65 for benzene ion and m/z 81, 53, 54 for pyrazine ion will be discussed later in section 3.2.3. To compare the relative difference in energy deposition for the various surfaces quantitatively, the extended deconvolution method⁽⁴⁰⁾ was applied to calculate the percentage of the average T→V transfer (calculated from internal energy distribution diagrams for benzene at 30 eV collision energy). Conversion of kinetic energy to internal energy of the benzene ion has the highest efficiency on the C12Br surface (11.6 ± 0.4 eV), followed by the C12F10 (10.3 ± 0.6 eV), C12Cl (9.5 ± 0.4 eV) \approx C14F1 (9.3 ± 0.4 eV), and C12 (5.8 ± 0.6 eV) surfaces. These values are plotted in Figure 3.7. As mentioned previously, more efficient energy deposition can be attributed to higher surface rigidity or the higher effective mass of the terminal group. There is no clear definition of surface rigidity at this time. The order of surface rigidity for the surfaces studied here can be arranged in the order of C12F10 > C14F1 \approx C12Br \approx C12Cl \approx C12 by the following argument. The C12F10 surface has the highest rigidity due to its rigid helical (CF₂)_n backbone compared to surfaces with all trans-

Figure 3.5. Product ion spectra with benzene projectile ion (m/z 78) colliding with (a) C₁₄F₁, (b) C₁₂Cl, (c) C₁₂Br, and (d) C₁₂ surfaces at 30 eV collision energy. Product ions with m/z greater than m/z 78 correspond to addition products formed by reaction of the projectile with surface chains.

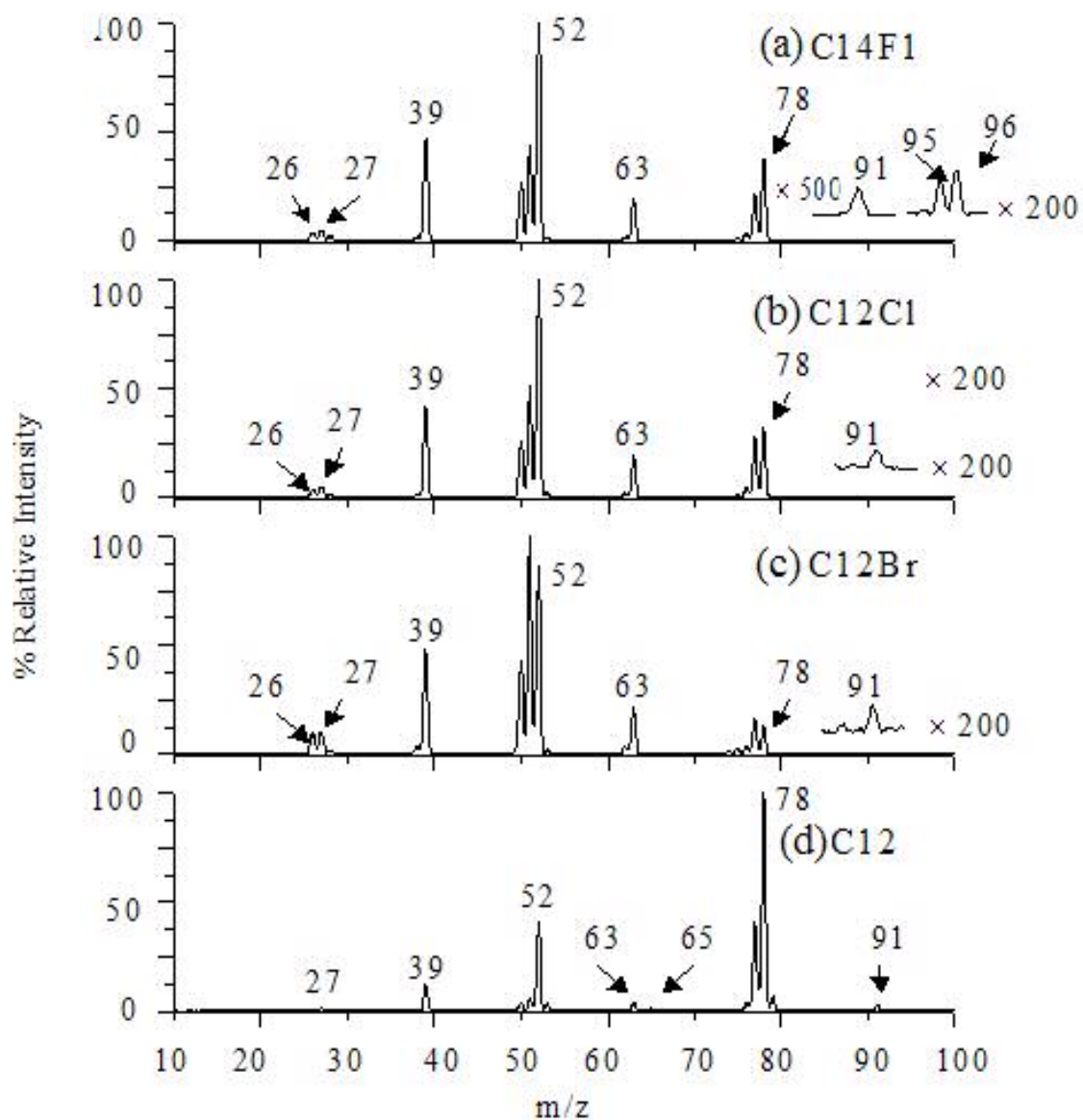


Figure 3.6. Product ion spectra for pyrazine projectile ion (m/z 80) colliding with (a) C₁₄F₁, (b) C₁₂Cl, (c) C₁₂Br, and (d) C₁₂ surfaces at 20 eV collision energy. The peak at m/z 81 is the hydrogen addition product formed by abstraction of hydrogen atom from the SAM films, and that at m/z 54 corresponds to the loss of HCN.

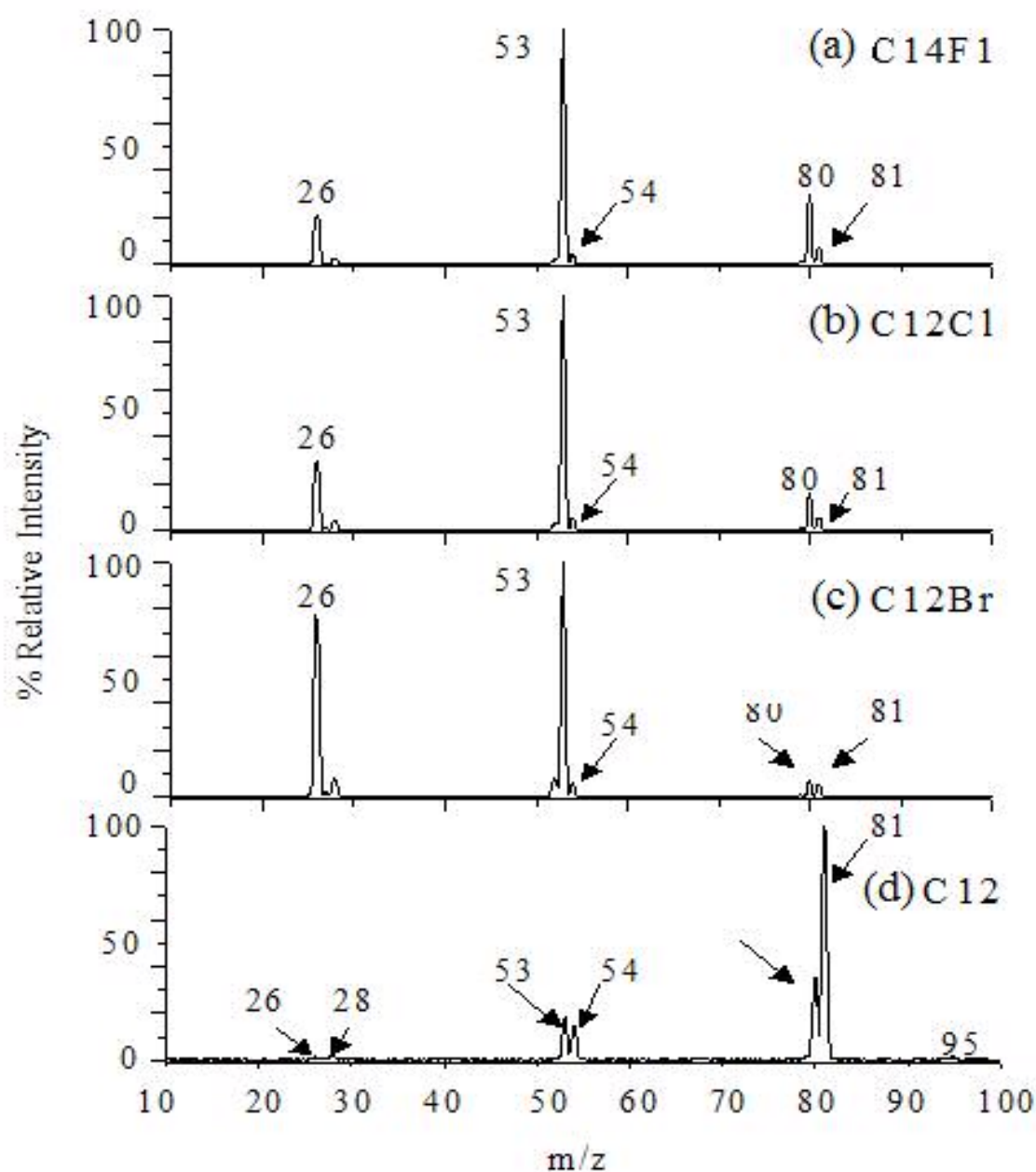
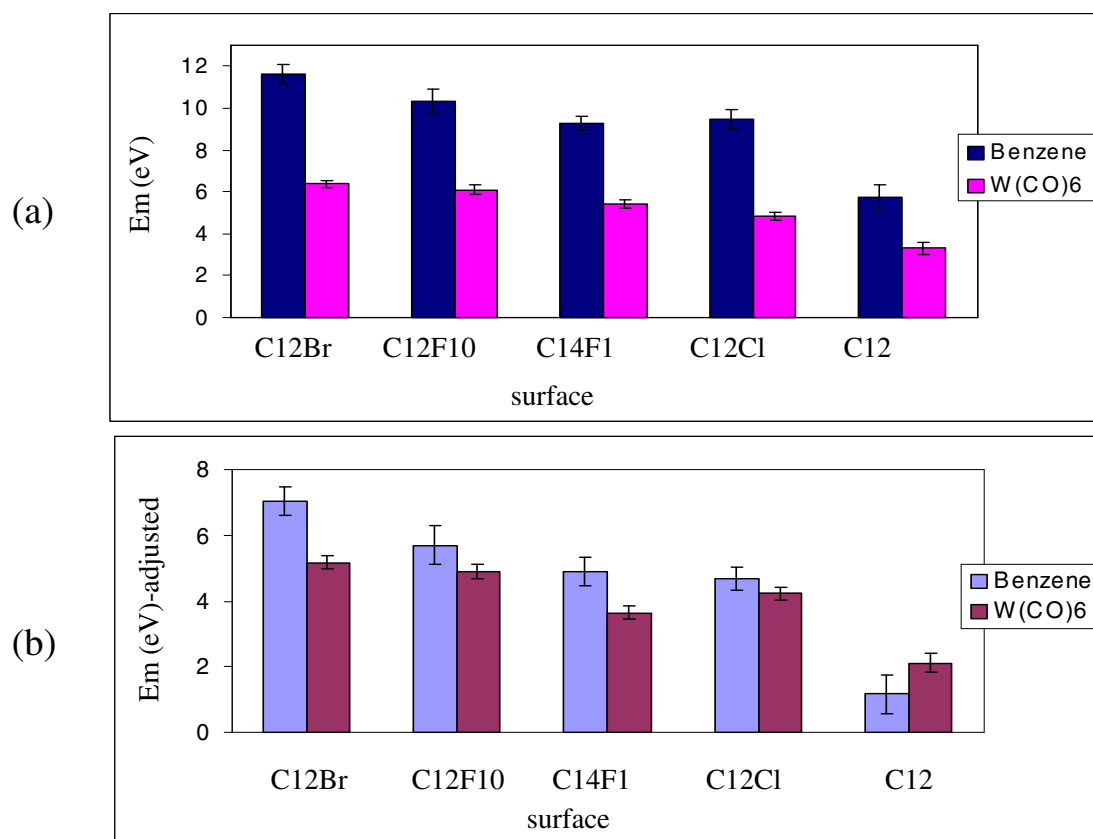


Figure 3.7 Comparison of mean energy deposition E_m (relative to the collision energy 30 eV) for C12Br, C12F10, C14F1, C12Cl and C12 surfaces with benzene and $W(CO)_6$ as projectile ions. (a) original values calculated by extended deconvolution method for benzene⁽⁴⁰⁾ and by algorithm for $W(CO)_6$.⁽³²⁾ (b) original value for benzene and adjusted value for $W(CO)_6$ by adding the first appearance energy difference between benzene (4.6 eV) and $W(CO)_6$ (1.2 eV) from values shown in (a).



$(\text{CH}_2)_n$ backbones.⁽¹⁰⁹⁾ The other four surfaces have similar surface rigidity because they have the same $(\text{CH}_2)_n$ backbone. The terminal group may affect surface rigidity but this effect is small compared to the effect of the backbone. Because the surface rigidity order is not consistent with the fact that the C12Br surface has higher energy deposition than either the C12F10 or the C14F1 surfaces, it is not the dominant factor. The masses of the terminal groups for the surfaces studied here increase in the order of CH_3 (15) < CH_2Cl (49) < CF_3 (69) < CH_2Br (94), if the terminal group is defined as the terminal carbon and its attached atoms. The order of mass of terminal groups basically agrees with the experimental results except that C12Cl and C14F1 have very similar energy deposition. Because previous studies in our group have suggested that the terminal carbon with its attached atoms mainly determines energy deposition,^(41,51,91) it was used to calculate the terminal as a start. The mean internal energy deposited to benzene ion was plotted against terminal group masses and the resulting plot is shown in Figure 3.8 (a). It can be seen that there is a good linear relationship between the deposited internal energy and the terminal group mass, which strongly supports that idea that the terminal mass is the major contributor to energy deposition. The linearity is not surprising if the energy transfer process is considered through the momentum transfer pathway. The fragmentation patterns produced with $\text{W}(\text{CO})_6^+$ projectile ions were also used to estimate the percentage of kinetic to internal energy transfer. $\text{W}(\text{CO})_6^+$ is well known as a good “thermometer ion” due to its well established unimolecular dissociation pattern and energies.^(8,32) The product ion spectra of $\text{W}(\text{CO})_6^+$ at 30 eV collision energy on C14F1, C12Cl, C12Br, and C12 surfaces are illustrated in Figure 3.9. The increase in the

Figure 3.8. Plots of mean internal energy deposition versus terminal group mass of the C12F10, C14F1, C12Cl, C12Br, and C12 surfaces assuming that the terminal group is defined by the terminal carbon and its attached atoms. (a) benzene projectile ion (b) W(CO)₆ projectile ion.

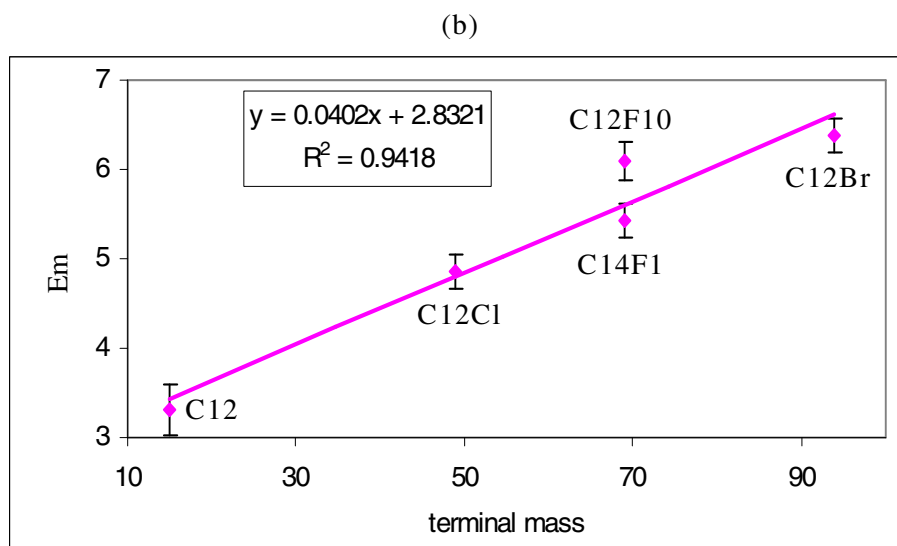
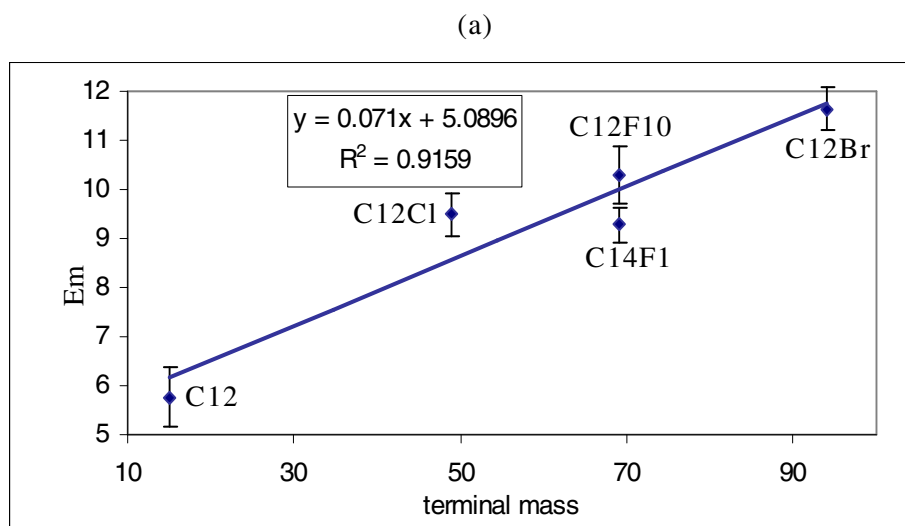
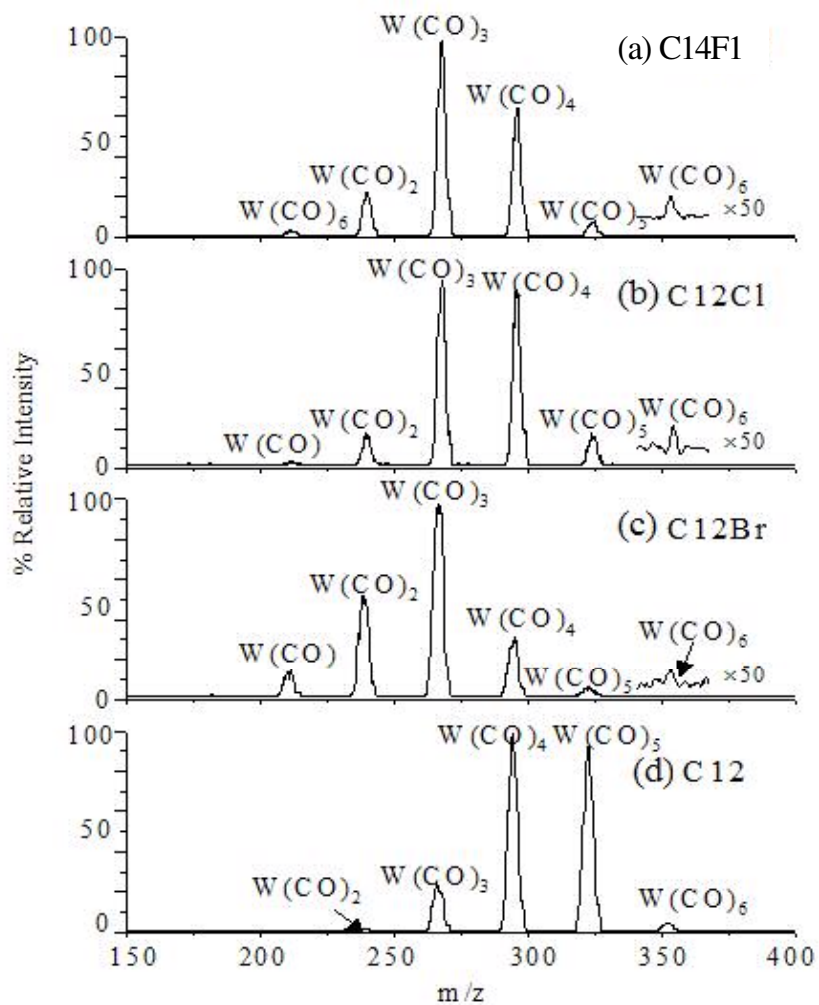


Figure 3.9. Product ion spectra with $W(CO)_6^+$ projectile ion colliding with (a) C14F1, (b) C12Cl, (c) C12Br, and (d) C12 surfaces at 30 eV collision energy.



projectile ion's internal energy deposition is demonstrated by the increasing abundance of lower mass fragments. The internal energy deposited into $W(CO)_6^+$ ions was estimated using an algorithm published by Cooks and coworkers⁽³²⁾ and plotted as a bar graph in Figure 3.7 (a). $T \rightarrow V$ decreases in the order of C12Br (6.4 ± 0.2 eV) > C12F10 (6.1 ± 0.2 eV) > C14F1 (5.4 ± 0.2 eV) > C12Cl (4.9 ± 0.2 eV) > C12 (3.3 ± 0.3 eV), which is also consistent with the order of terminal mass. It is clear that there is a good linear relationship between the energy deposition and the terminal mass. This again proved that terminal mass is the dominant factor for energy deposition.

Another phenomenon that needs to be pointed out is benzene ions always deposit more energy to its internal energy than the $W(CO)_6$ ions, even on the same surfaces. This can be explained by the excess internal energy of each prior to collision. The first appearance energy for fragmentation of benzene is 4.6 eV⁽⁴⁰⁾ above the ionization energy and is 1.2 eV for $W(CO)_6$ ion.⁽³²⁾ This means that benzene ion obtains 3.4 eV higher internal energy from the EI source than the $W(CO)_6$ ion. If we correct the energy deposition values for these excess energies, the two ions show similar energy deposition as shown in Figure 3.7 (b).

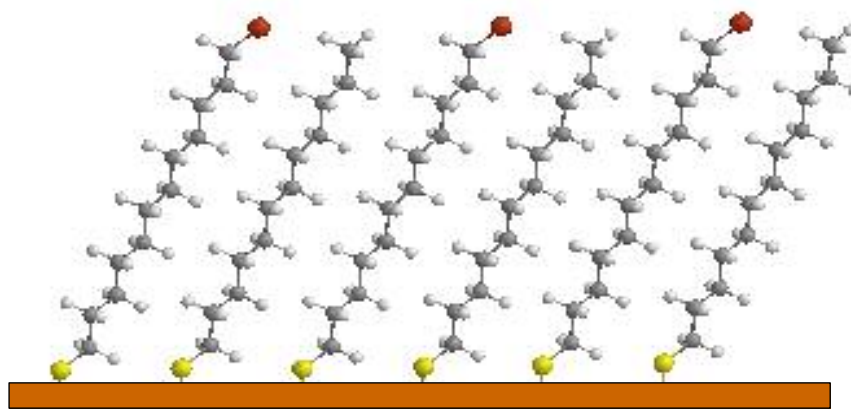
C12Cl and C12Br surfaces diluted with C12 and C11 were used to provide complementary information for understanding the energy deposition, *e.g.* speculation that C12 and C11 dilution might relieve crowd of the CH_2Cl or CH_2Br terminal groups. The diluted surfaces were prepared by incubating gold surfaces in 50:50 (mole fraction) mixed solution of 1 mM C11 or C12 thiol with 1 mM C12Cl or C12Br thiol for 24 hours.

The total concentration of the mixed solution is 1 mM. C12 has the same chain length while C11 is one carbon shorter than the C12Cl and C12Br chains. For C11 diluted surfaces, CH₃ terminal groups on C11 chains may be partially shielded by the lone pairs on the adjacent CH₂Cl or CH₂Br groups which prevents the projectile ions from interacting with the CH₃ groups. The C11 diluted surfaces show higher energy deposition than the C12 diluted ones presumably due to more exposed CH₂Cl or CH₂Br groups. Figure 3.10 demonstrates the above scenario using C12Br mixed SAMs as an example. The relative energy deposition was plotted versus the percentage of C12Cl or C12Br in solution and is presented in Figure 3.11.

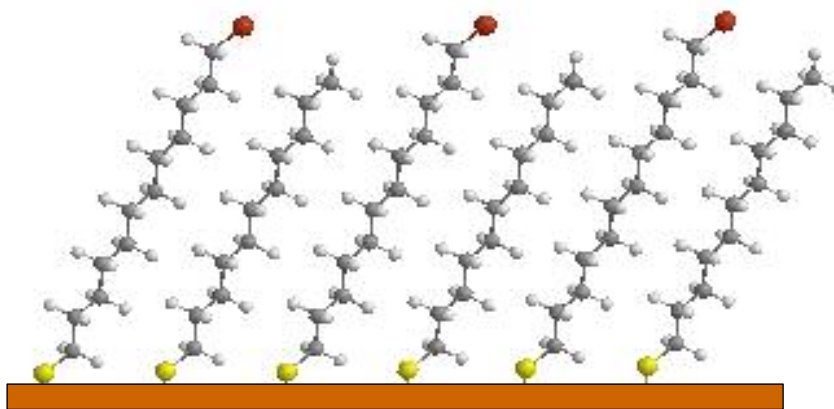
3.2.2 Electron transfer

Neutralization of projectile ions presumably occurs by electron transfer through the SAM film during the ion-surface collision process although the exact mechanism is not known for various projectile-surface combinations. A plot of the total ion current (TIC) for a set of surfaces with pyrazine molecular ions as projectiles at 20 eV collision energy is presented in Figure 3.12. The baseline in Figure 3.12 was obtained when the filaments of the ion source were turned off. The total ion current is the total scattered ions detected at the electron multiplier after surviving the collision at the surface and includes all the ions appearing in the product spectrum, that is, the intact precursor ions, fragment ions, and reaction product ions. A higher TIC value in the plot indicates less electron transfer or less projectile ion neutralization. It is clear that the efficiency in electron transfer from the films on gold to the pyrazine molecular ion follows the order C14F1 <

Figure 3.10. ChemDraw 3D demonstration of difference between C11 and C12 diluted C12Br surfaces. C12Br:C11 (50:50) surface has more exposed CH₂Br group and less exposed CH₃ group than C12Br:C12 (50:50) surface. More exposed is defined as greater height difference between adjacent groups.



C12Br:C12 (50:50)



C12Br:C11 (50:50)

Figure 3.11. Comparison of estimated average internal energy deposited into (a) benzene and (b) $W(CO)_6$ projectile ions on C12 and C11 diluted C12Cl (i) and C12Br (ii) surfaces as a function of their concentrations in solution. C11 diluted surfaces always show higher energy deposition than the C12 diluted ones. Points are connected with best fit lines to highlight the difference between C11 and C12 diluted surfaces. Diamonds represent C12 diluted surfaces, squares represent C11 diluted surfaces.

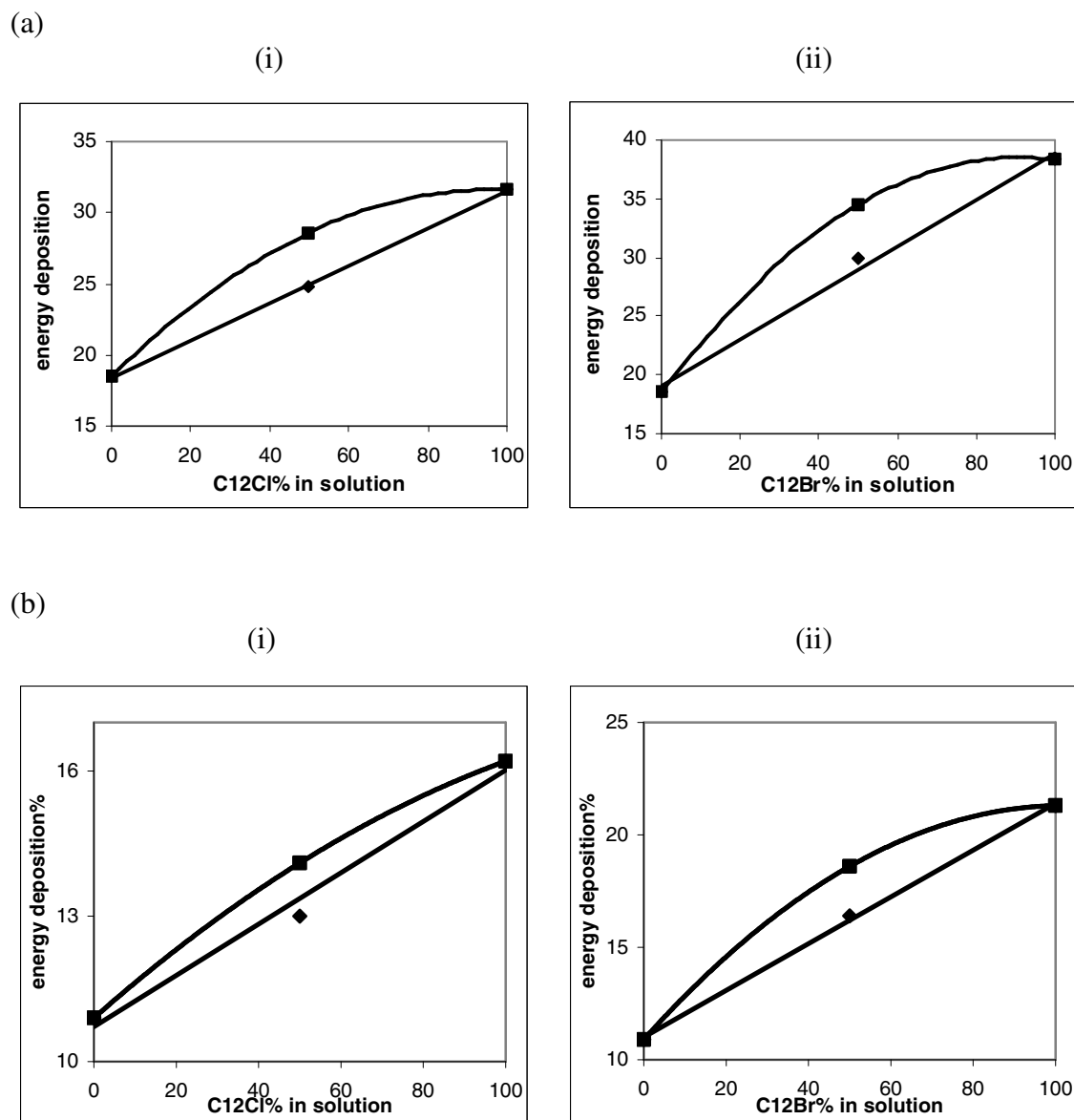
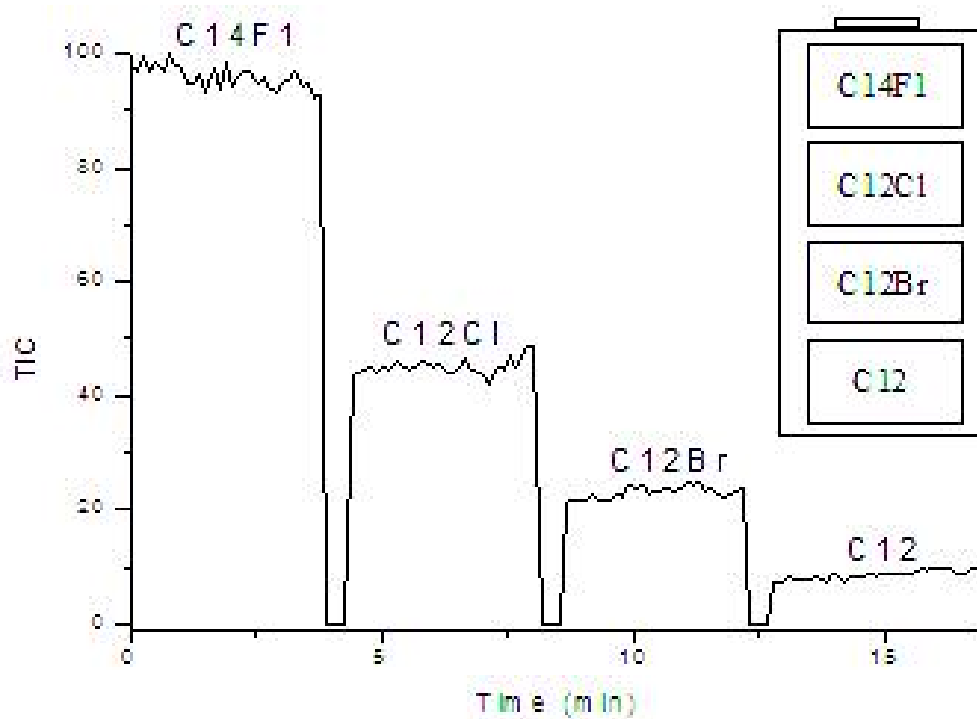
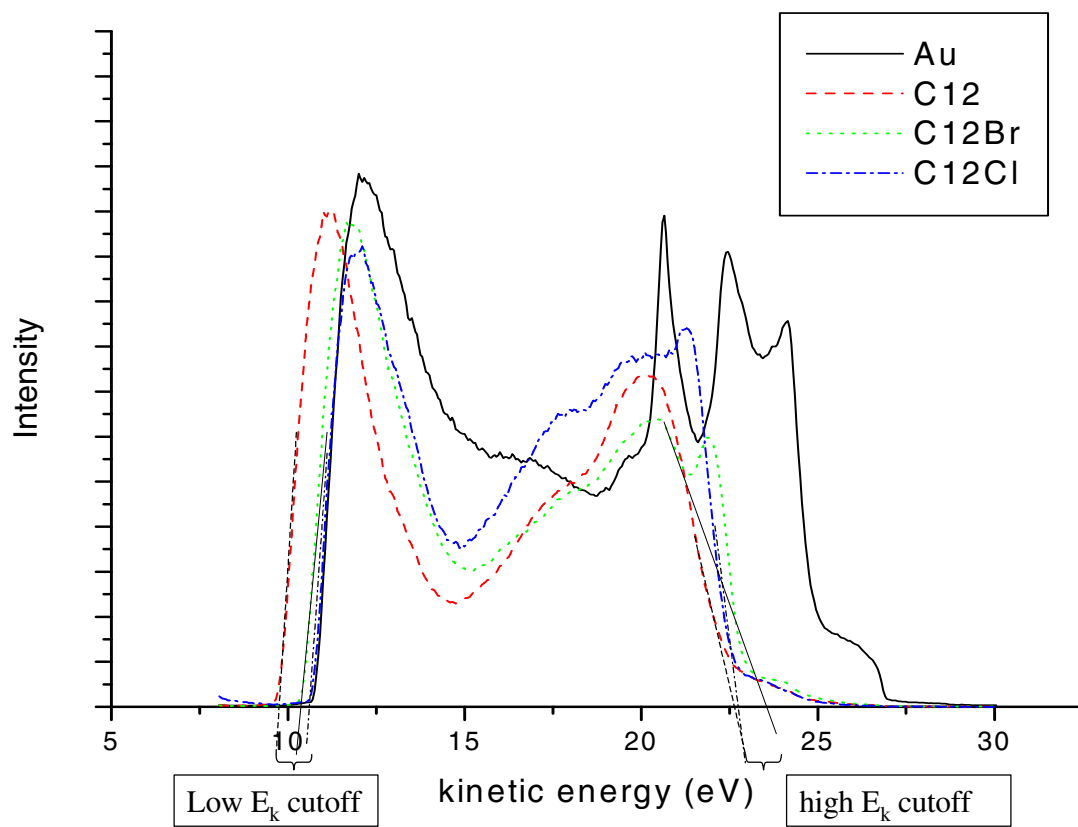


Figure 3.12. Total ion current surviving collision with C14F1, C12Cl, C12Br, and C12 surfaces using pyrazine projectile ion at 20 eV collision energy.



$C12Cl < C12Br < C12$. The same results were achieved when using benzene as projectile ions. According to one of the mechanisms mentioned above, electron transfer from the SAM film on Au to incoming ions is speculated to be roughly related to both the ionization energy of the SAM film and the recombination energy of the projectile ion. For the same projectile ion, electron transfer is mainly determined by the ionization energy of the SAM surface. Films with lower ionization energy show more facile electron transfer which will facilitate the neutralization of incoming ions. The second theory states that vacuum-surface interface dipole affects the electron transfer. Positive dipoles such as in an HSAM decrease the energy level and allows electrons to transfer from the film more easily. Conversely, negative dipoles such as in an FSAM increase the energy level and hinder the escape of the electrons from the film. Which of the two mechanisms contributes for all the surfaces as well as ionization energies and the surface-vacuum interface dipoles estimated from UPS measurements. The UPS spectra for C12Cl, C12Br, C12 films on gold foil, and bare gold foil plotted as intensity (counts/sec) versus the kinetic energy of the ejected electrons (eV) are shown in Figure 3.13. Electrons with highest E_k , *e.g.* around 26.9 eV on plot, are from the gold Fermi edge (valence edge) and this energy remains the same for all of the surfaces. Electrons with higher E_k , *e.g.* 23.6 eV for C12Br, 22.7 eV for C12Cl, and 22.6 eV for C12 are high kinetic energy cutoff, and electrons with lower E_k , *e.g.* around 10.3 eV for C12Br, 10.2 eV for C12Cl, and 9.3 eV for C12 are high kinetic energy cutoff, both of the features originate from the adsorbed monolayer. The estimated IE of a SAM surface is calculated by the equation:

Figure 3.13. UPS spectra for clean Au and C12Cl, C12Br, C12 surfaces on Au foil.



$$IE = hv - (\text{high } E_k \text{ cutoff} - \text{low } E_k \text{ cutoff}) \quad \text{Eq. 3}$$

where hv is the photon energy (21.2 eV for He I).

Interface dipoles were estimated according to the method reported in reference 46. Briefly, equation 4 was used to describe the changes in surface potential upon adsorption of an alkanethiol monolayer on the metal substrate assuming well ordered dipoles:

$$\Delta U = N (\mu_{\text{mol},\perp}/\varepsilon - \mu_{\text{Au-S}}) \quad \text{Eq. 4}$$

where ΔU is the change in surface potential upon surface modification, N is the areal density of molecules (typically ca. $(3-5) * 10^{-14} \text{ cm}^{-2}$), $\mu_{\text{mol},\perp}$ is the dipole moment of an individual molecule in the thin film normal to the surface, $\mu_{\text{Au-S}}$ is the dipole moment of Au-S bond, and ε is the dielectric constant of the molecular layer which typically is estimated to be ca. 2-3. The areal density of molecules, dipole moment of Au-S bond, and the dielectric constant are constant, therefore the dipole moment of an individual molecule is directly correlated to the change in surface potential. The calculated dipole moments of the individual alkanethiols were used as an estimate of the sum of molecular dipoles of the SAM surfaces. The dipole moments of individual molecules were calculated using Gaussian 03.

Electron transfer from SAM surface to projectile ions can be speculated as a similar process to electron transfer from SAM surface to the tip in scanning probe microscopy (SPM) measurement experiment. When the tip approaches the surface with a changing bias voltage, current flows across the SAM film.⁽¹¹⁰⁾ There is no current when the tip was not in contact with the SAM film. The current i can be described by the empirical relation⁽¹¹⁰⁾:

$$i = i_0 \exp(-\beta d) \quad \text{Eq. 5}$$

where i_0 is the preexponential factor, d is the distance between the tip and the metal substrate, and β is a structure-dependent attenuation factor that describe the decay of electronic coupling between the tip and the metal substrate. Assuming that the projectile ions can be considered to play the same role as the tips in SPM, total ion current flow through the SAM films should depend exponentially on the electronic property of the SAM film molecules based on the above relationship.

TICs for the benzene projectile ion were plotted versus the ionization energy of the surfaces and surface-vacuum interface dipoles in Figure 3.14 and TIC for pyrazine projectile ion were plotted in Figure 3.15. It can be seen that the TIC has a better exponential relationship with interface dipole than with the ionization energy, so interface dipole of the SAM film plays a more dominant role in neutralization. Gas-phase UPS data were obtained for comparison with the thin-film UPS spectra and are shown in Figure 3.16. The sharp peak at IE about 9-10 eV is due to the ionization of a sulfur 3p lone pair orbital. This peak shifts to higher IE on the C12F10 surface due to the introduced C-F bonds and dipole that pointing from Au to the CF₃ terminal group. In most cases various conformations of the molecules are present in both gas-phase and thin-film spectra.⁽⁴⁶⁾ In the gas-phase spectra, the broad featureless band at ca. 10-17 eV is the alkyl C-C and C-H σ bond ionizations. The IE obtained from gas-phase UPS are listed in Table 3.2. It's clear that IE from thin-film spectra are lower than that from gas-phase spectra. This can be attributed to photoionization in a condensed phase environment and the polarization of that environment to screen the core-hole charge

Figure 3.14. Relationship between the total ion current for benzene projectile ion and (a) surface ionization energy and (b) surface interface dipole calculated from UPS spectra. Curves indicate the best exponential fit obtained for the data.

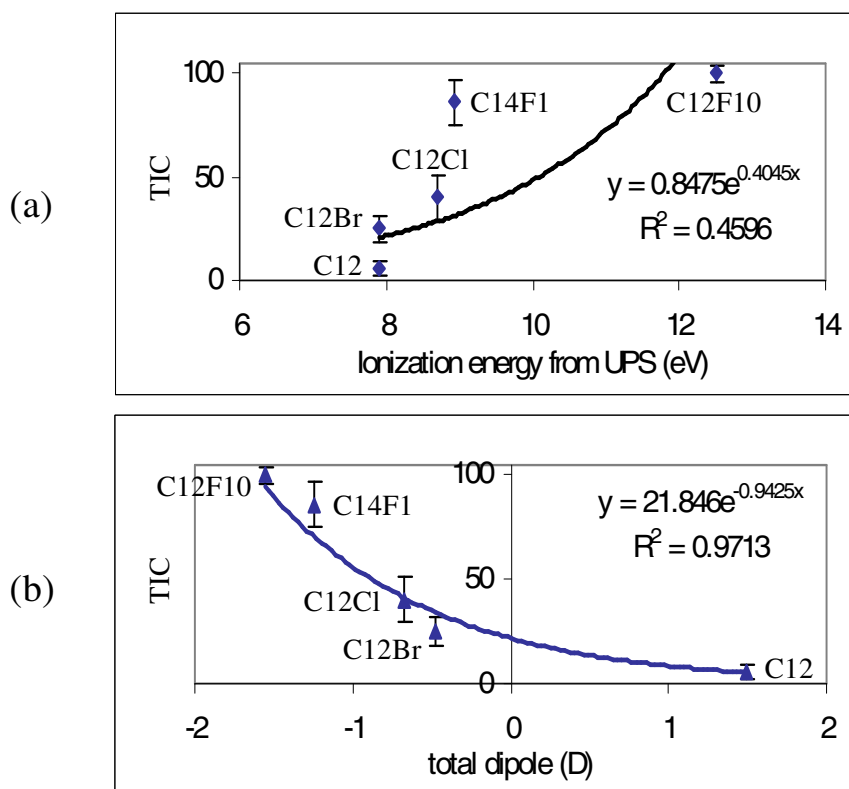


Figure 3.15. Relationship between the total ion current for pyrazine projectile ion and (a) surface ionization energy and (b) surface interface dipole calculated from UPS spectra. Curves indicate the best exponential fit obtained for the data.

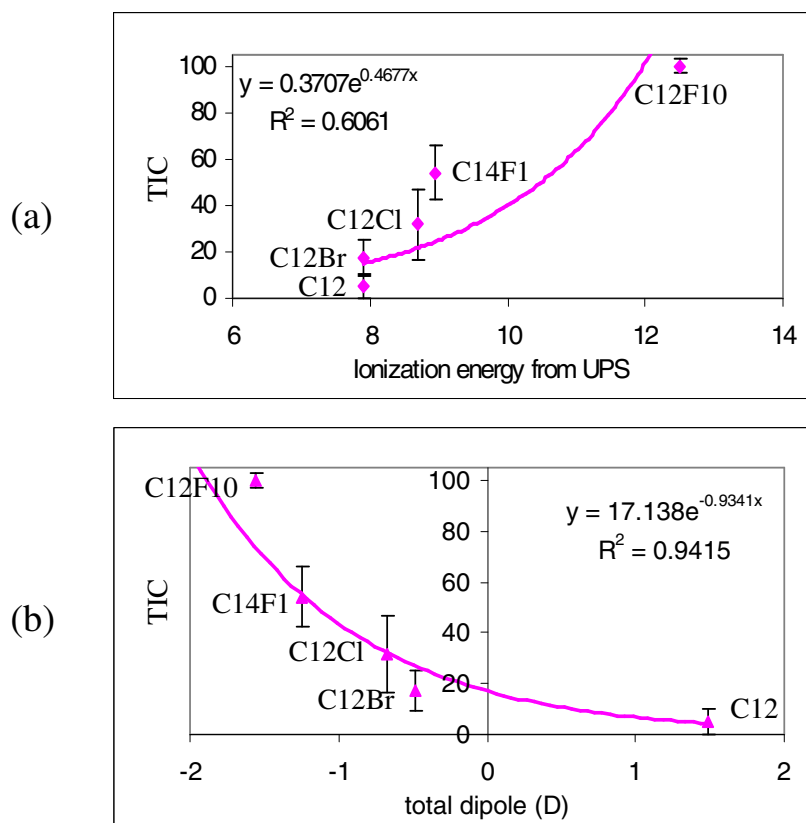


Figure 3.16. Gas-phase UPS spectra for C12F10, C12, C12Cl, and C12Br surfaces. The sharp peak at low IE arises from the ionization of the sulfur lone pair orbitals (marked by (*)).

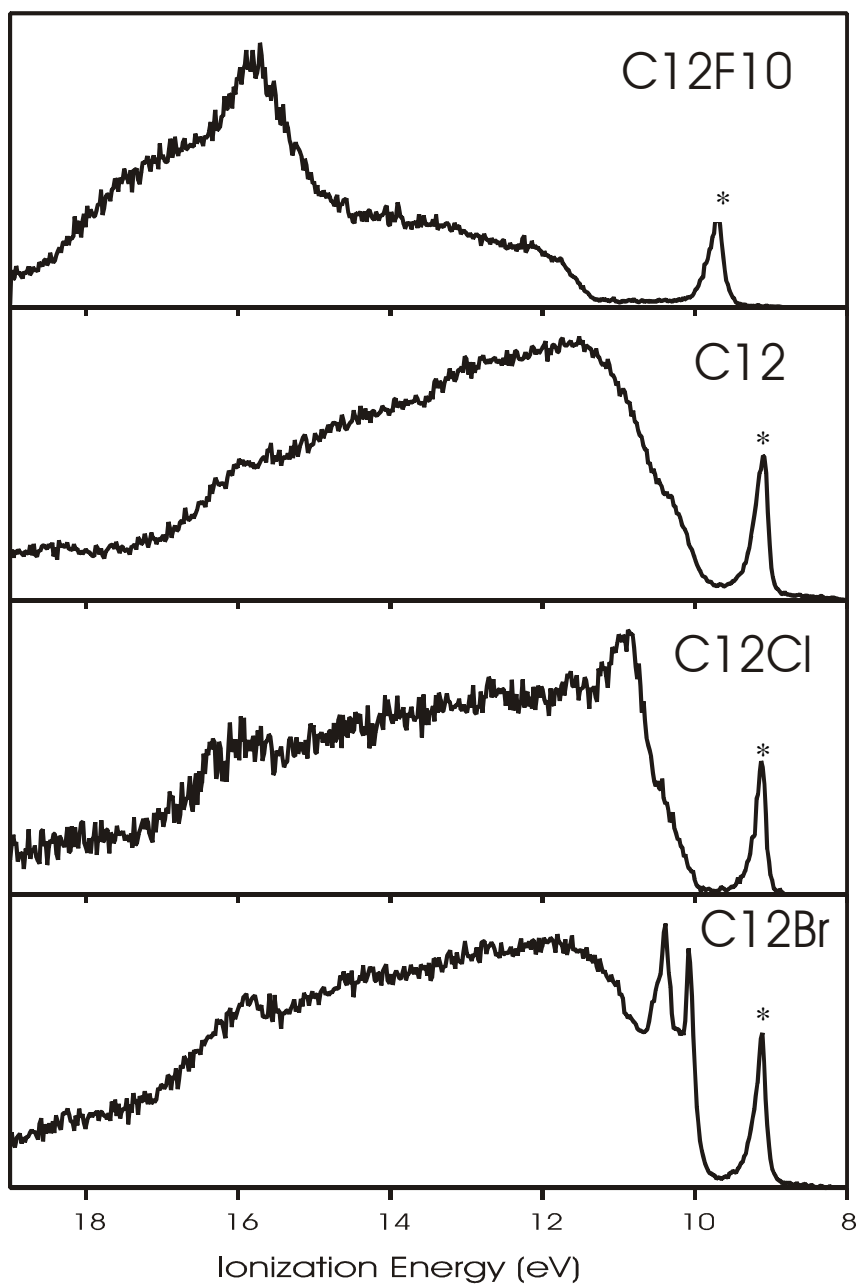


Table 3.2. Ionization energy, interface dipole (from UPS), and TIC for C12F10, C14F1, C12Cl, C12Br, and C12 surfaces.

Surface	C12F10	C14F1	C12Cl	C12Br	C12
IE (eV) from UPS	12.5	8.94	8.7	7.9	7.9
IE (eV) from gas-phase UPS	14.4	N/A	10.4	9.9	9.8
Interface dipole (D)	-1.56	-1.25	-0.68	-0.48	1.49
TIC-benzene	100	78.4	40.2	25.1	5.2
TIC-pyrazine	100	54.2	31.8	17.4	5.0

created in the photoemission event.⁽¹¹¹⁾

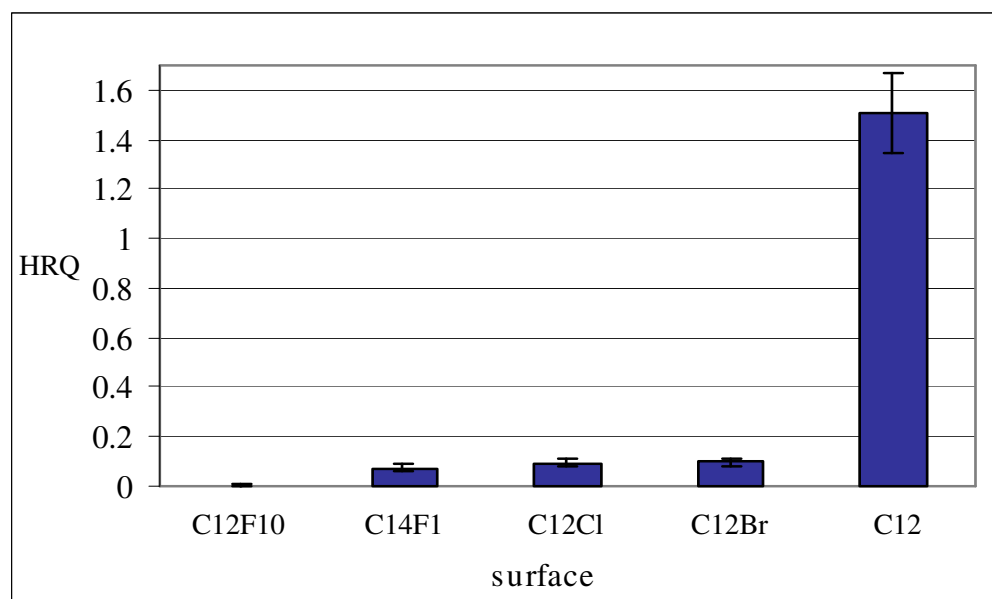
3.2.3 Ion-surface reactions

Benzene molecular ions (m/z 78) have been shown to be good probes to investigate the fluorine abstraction from FSAMs versus hydrogen abstraction from HSAMs.⁽⁴⁷⁾ Benzene ions are used as projectiles here to see if they could abstract a Cl atom or CH_2Cl group from the C12Cl surface or abstract a Br atom or CH_2Br group from the C12Br surface happens. Figure 3.5a shows fluorine-abstraction products formed during collisions with benzene ions at 30 eV collision energy. Upon colliding with the C14F1 surface, there are mainly two reaction products formed, $\text{C}_6\text{H}_6^+ + \text{F} - \text{H} = \text{C}_6\text{H}_5\text{F}^+$ (m/z 96) and $\text{C}_6\text{H}_6^+ + \text{F} - \text{H}_2 = \text{C}_6\text{H}_4\text{F}^+$ (m/z 95) (Figure 3.5a). When benzene molecular ions collide with a CH_3 -terminated SAM, it produces the reaction ion $\text{C}_6\text{H}_6^+ + \text{CH}_3 - \text{H}_2 = \text{C}_7\text{H}_7^+$ (m/z 91) which can undergo further fragmentation to produce C_5H_5^+ (m/z 65). There is also a weak m/z 91 peak at for the C14F1 surface that is absent for the C12F10 surface. A reasonable explanation is that some projectile ions are able to penetrate through the terminal group and access underlying CH_2 groups.⁽⁴¹⁾ No reaction product

was observed resulting from Cl abstraction from the C12Cl surface or Br abstraction from the C12Br surface. The m/z 91 peak observed on C12Cl surface can be explained by $C_6H_6^+ + CH_2Cl - HCl = C_7H_7^+$ and that on C12Br surface could be explained by $C_6H_6^+ + CH_2Br - HBr = C_7H_7^+$.

Pyrazine ions have been shown to form abundant H addition products when colliding on hydrocarbon SAMs.⁽⁴¹⁾ The ion-surface reaction products achieved using pyrazine molecular ions (m/z 80) on C14F1, C12Cl, C12Br, and C12 surfaces are shown in Figure 3.6. On all the surfaces, reactions occur between the pyrazine molecular ion and the available hydrogen atoms. These reactions give rise to $C_4N_2H_4^+ + H = C_4N_2H_5^+$ (m/z 81) ions, and the $C_4N_2H_4^+$ (m/z 80) and $C_4N_2H_5^+$ (m/z 81) ions can gain sufficient internal energy to lose a neutral HCN and fragment to m/z 53 and m/z 54, respectively⁽⁴¹⁾. Similar to benzene projectile ion, the m/z 81 peak on the C14F1 surface is also for hydrogen abstraction from the $(CH_2)_n$ backbone group under the terminal group. For the C12 surface, there is another reaction product formed by $C_4N_2H_4^+ + CH_3 = C_5N_2H_7^+$ (m/z 95). A hydrogen reaction quotient (HRQ) $[(MH^+ + (MH - HCN)^+)/ (M^+ + (M - HCN)^+)]$ or in terms of m/z values $[(81+54)/(80+53)]$ can be calculated by using the integrated normalized peak areas of the corresponding ions.⁽⁹¹⁾ The HRQs calculated for all the surfaces are plotted as a bar graph in Figure 3.17. The C12 surface has the highest HRQ due to the easily accessible H atoms from the terminal CH_3 groups. The C12F10 surface and the C14F1 surface have low HRQ because they do not have H atoms in their terminal groups. The C12F10 surface shows even lower hydrogen addition than the C14F1 surface due to the deeply buried CH_2 groups compared to those on the C14F1 surface. Any

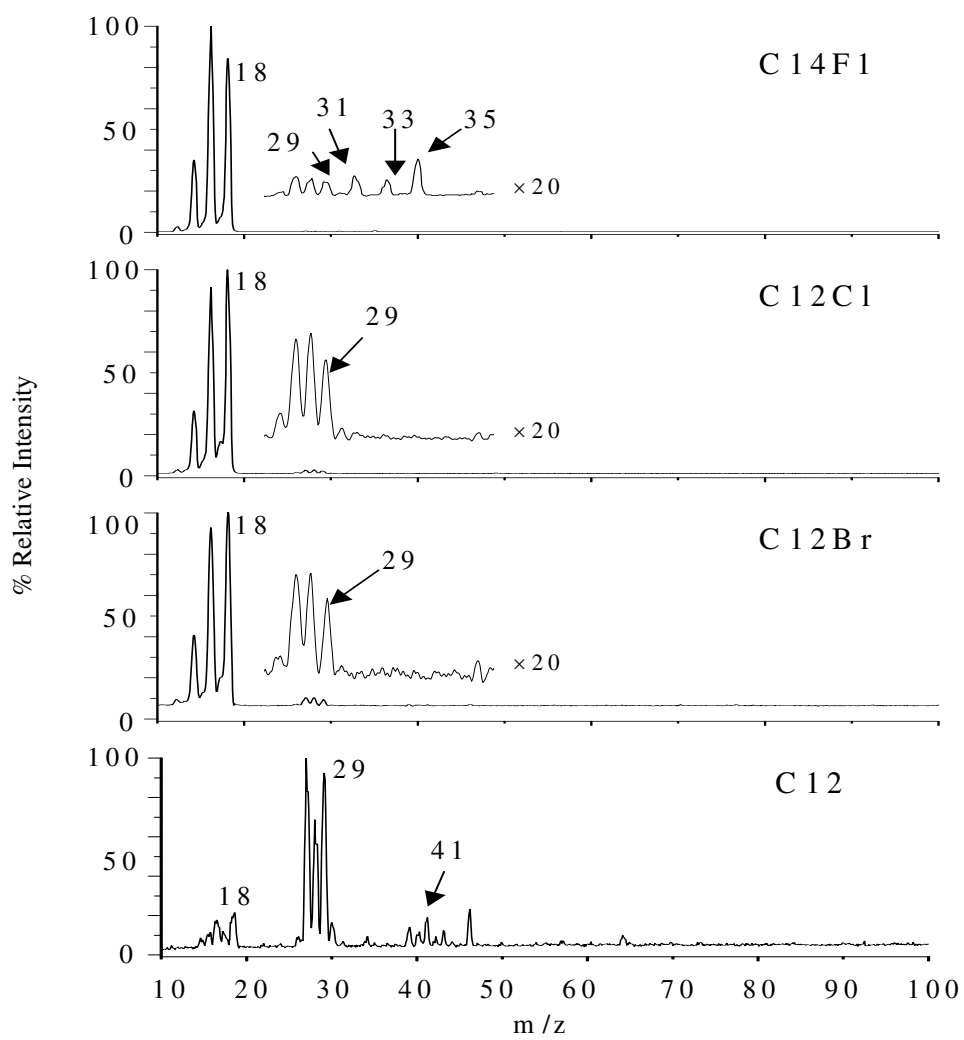
Figure 3.17. The comparison of hydrogen addition quotient (HRQ) for C12F10, C14F1, C12Cl, C12Br, and C12 surfaces.



hydrogen addition on C12F10 surface is likely the result of surface damage and contamination. The C12Cl surface and the C12Br surface show similar hydrogen additions, both are smaller than hydrogen addition from hydrocarbon surfaces and larger than that from the partially fluorinated C14F1 surface. C11 and C12 diluted surfaces were also used to study ion-surface reactions. C12 diluted surfaces have more hydrogen reaction than the C11 diluted ones, indicating more available hydrogen atoms from more exposed CH₃ terminal groups. This is noteworthy because typically an even chain length, single component film would give great hydrogen addition because of the perpendicular orientation of the terminal C-H bond.

CD₃⁺ projectile ions were used to further investigate the ion-surface reaction since it has been reported to abstract H⁻ and CH₃⁻ from the CH₃-terminated surface, and F⁻ from the fluorinated surface.⁽⁹⁸⁾ It is possible that the CD₃⁺ ion might abstract Cl from the C12Cl surface or Br from C12Br surface. The product ion spectra obtained with CD₃⁺ ion at 30 eV collision energy are presented in Figure 3.18. The spectrum for the C14F1 surface is dominated by CD₃⁺ ions (m/z 18) and its fragments, CD₂⁺ (m/z 16) and CD⁺ (m/z 14). The small peaks at m/z 35, 33, and 31 are fluoride addition products and subsequent fragmentations, that is, [CD₃⁺ + F - D]⁺, [CD₃⁺ + F - D₂]⁺, and CF⁺, respectively. For the C12Cl and C12Br surfaces, CD₃⁺ ions and its fragments still dominate, but the fluoride addition and its fragment ions are missing as expected and some sputtered ions (alkyl chain fragments from the surface) appear with low intensity, C₂H₃⁺ (m/z 27), C₂H₅⁺ (m/z 29). The CD₃⁺ ions and its fragments have lowest

Figure 3.18. Product ion spectra obtained by colliding CD_3^+ projectile ion with C_{14}F_1 , C_{12}Cl , C_{12}Br , and C_{12} surfaces at 30 eV collision energy.



intensity while the sputtered ions have the highest intensity in the C12 surface spectrum. No Cl or Br abstraction product ions were observed on the C12Cl or C12Br surfaces, but this does not rule out the possibility of Br⁻ or Cl⁻ abstraction which could produce neutral CD₃Cl or CD₃Br and an ionized chain.

3.3 Conclusions

In the present study, chlorine and bromine terminated films were compared with HSAMs and FSAMs to study some important processes that occur during low energy ion-surface collisions. The conversion of kinetic energy to internal energy for the polyatomic projectile ions shows a good linear relationship with the mass of the terminal group which suggests that energy transfer depends on mainly the terminal carbon and its attached atoms. Benzene ions always show apparent higher energy deposition than W(CO)₆ ions on the same surfaces, which can be attributed to their excess internal energy before surface collision. The magnitude of this excess is greater for benzene because appearance energy for formation of the lowest energy fragment of benzene is high (4.6 eV). Although it has been suggested that the ionization energy of the surface plays an important role in electron transfer through the organic film, our research shows that the surface interface dipole contributes more to the electron transfer process. It is shown here that electron transfer has a good exponential relationship with the surface interface dipole. Consistent with previous work in this group, ion-surface reactions are predominantly determined by the nature of the terminal group as demonstrated by the hydrogen addition reaction difference among these surfaces. For C12Cl or C12Br surfaces, no charged Cl abstraction or Br abstraction products were observed with

benzene, pyrazine or CD_3^+ projectile ions although abstraction of Br^- or Cl^- (in parallel to H^- and CH_3^- abstraction from hydrocarbon films) to form neutral products can not be ruled out.

Chapter 4. Development of Soft Landing as a Method for Separation

4.1 Introduction

Soft landing is defined as the intact deposition of gas phase polyatomic ions onto an appropriate surface at low collision energy.^(112,113) Simple organic cations,⁽¹¹²⁾ metal clusters,⁽¹¹⁴⁾ polysaccharides,⁽¹¹⁵⁾ nucleotides,⁽¹¹⁶⁾ viruses,⁽¹¹⁷⁾ and proteins^(38,118,119) have all been soft-landed molecules. Typical collision energies used are ~ 1 -13eV. Low collision energies are preferred to suppress surface-induced dissociation as well as ion-surface reactions. It should also be pointed out that too low an energy results in difficulties in focusing the ion beam and an increase in reflection.

One early example of soft landing is the deposition of $(\text{CH}_3)_2\text{SiNCS}^+$ and variously substituted pyridine ions onto a fluorinated self-assembled monolayer (F-SAM, $\text{CH}_3(\text{CF}_2)_7(\text{CH}_2)_2\text{S}-$) at ~ 10 eV collision energy.⁽¹¹²⁾ The result that the intact ions can be trapped at the surface for long periods was explained by two facts: (i) the combination of steric hindrance in the polyatomic ions and the inert and ordered matrix formed by the FSAM, and (ii) the electrostatic interaction between the soft-landed ions and their induced electric dipoles at the surface.^(112,120) The electrostatic interaction was calculated to be ~ 2 eV, which is of the order of strong chemisorption.⁽¹¹²⁾

Sterically more bulky projectile ions were shown to be deposited more easily which can be explained by the “interwining” trapping mechanism.^(112,120,39) Specifically, the bulky substituents serve to increase the cross-section and remove translational energy from the projectile ions. They also help to lock ions into the film matrix and protect the

reactive site from other reagents. Letting the modified surface sit in vacuum resulted in loss of landed material, which maybe due to neutralization, reaction or adsorption of hydrocarbons or other species that exist in the instrument.⁽¹¹²⁾

The deposited polyatomic ions were present at the surface at least partially as charged species because of the following evidence.^(38,39,112,117-120) First, the projectile ions could be liberated intact by low energy sputtering and there was no evidence for products other than those from dissociation or reaction of deposited ions. Second, there was no correlation between the recombination energy of the projectile ion and the sputtered ion yield. The charged species may present a Coulombic barrier for further deposition and limit the amount of materials soft-landed because of the charge accumulation.

It was found that only closed-shell ions (even-electron ions) could be successfully soft-landed, the open-shell ions (radical ions) could not because the available unfilled orbital promotes electron transfer and precludes soft landing of the ion in its charged form.^(39,112)

The type of surface used for soft-landing is also important because its nature can determine the amount and chemical form of the deposited material.^(38,119) Shen and coworkers found that toluidine ions can be soft-landed more efficiently on a hydrocarbon SAM than on a F-SAM.⁽³⁹⁾ This is because a H-SAM surface is “softer” and causes less fragmentation upon ion collisions. They proposed that the H-SAM is potentially beneficial for depositing less stable ions that may dissociate readily at harder surfaces. Gologan *et al.* investigated the soft landing of proteins and peptides on F-SAM and glycerol/sucrose liquid surfaces.⁽¹¹⁹⁾ They observed a five-fold increase in soft-landing

efficiency on the liquid compared to that on the F-SAM throughout the energy range used. Not only the ion soft-landing efficiency, but the specific activity of soft-landed proteins were correspondingly higher. The difference in landing efficiency and residual bioactivity was explained as follows. When ions collide with the F-SAM, most of the ions undergo some conformational reorientation, in some cases unfolding, to expose the hydrophobic core to the substrate. The charges on the protein can, however, be isolated from the hydrophilic surface groups since the protein does not unfold completely. This leads to charge accumulation and prevents further soft landing of protein ions. On the other hand, protein ions undergo a series of low energy collisions with glycerol molecules on the liquid surface and part of their excess kinetic energy is removed. In addition, solvent molecules in the liquid provide some counterions to neutralize the protein charges which yields a neutral surface and facilitates further ion deposition. Another advantage is that polyols and sugars allow the capture and preservation of bioactivity.⁽¹²¹⁾

An exciting application of preparative soft landing mass spectrometry is its use as a separation method complementary to chromatography or electrophoresis.^(38,118,119) This application is particularly advantageous for molecules with highly similar structures but different molecular weights. In 2003, Ouyang *et al.* achieved protein microarrays by soft landing multiply protonated proteins.⁽³⁸⁾ An array of cytochrome C, lysozyme, insulin, and apomyoglobin was generated. The deposited lysozyme and trypsin retained their biological activity. After that, more protein separations and collections by soft-landing were performed by the Cooks' group.^(118,119) The aim of Cooks' work is to facilitate the development of this method as a protein microarray approach that can take full advantage

of the high resolution, sensitivity, automation and detection capabilities of current mass spectrometry.

The work in this chapter involves the soft landing of the peptide YGGFLR onto the C11OH, C11NH₂, and C12Br SAM surfaces. This project is being performed to determine whether the Extrel dual quadrupole instruments that exist in the Wysocki lab can be used without modification for soft landing. After these proof of concept experiments, further work on soft landing will be completed.

4.2 Experimental

The peptide YGGFLR was purchased from Sigma-Aldrich and used without further purification. Typical ESI conditions use 20 μM peptide solution in 70:30 methanol/water (volume ratio), 1% acetic acid, 3.7 kV applied to the syringe, and 1 μL/min sample flow (no nebulizing gas was used). The capillary temperature was set at 120°C, and the capillary voltage was 120 V. The surface was set normal to the entering ion beam during soft-landing. Soft-landing time was ~ 6-7 hr. After soft-landing, the soft-landed samples were rinsed with 70:30 methanol/water (volume ratio), 1% acetic acid solvent, collected and dried to ~ 5 μL. The sample was then sent to the Mass Spectrometry Facility at the Department of Chemistry, University of Arizona for MALDI analysis. The MALDI instrument used is Reflex III (Bruker, Billerica, MA, USA) time-of-flight mass spectrometer equipped with a reflectron and a 337 nm nitrogen laser.

4.3 Soft landing of YGGFLR on different SAMs

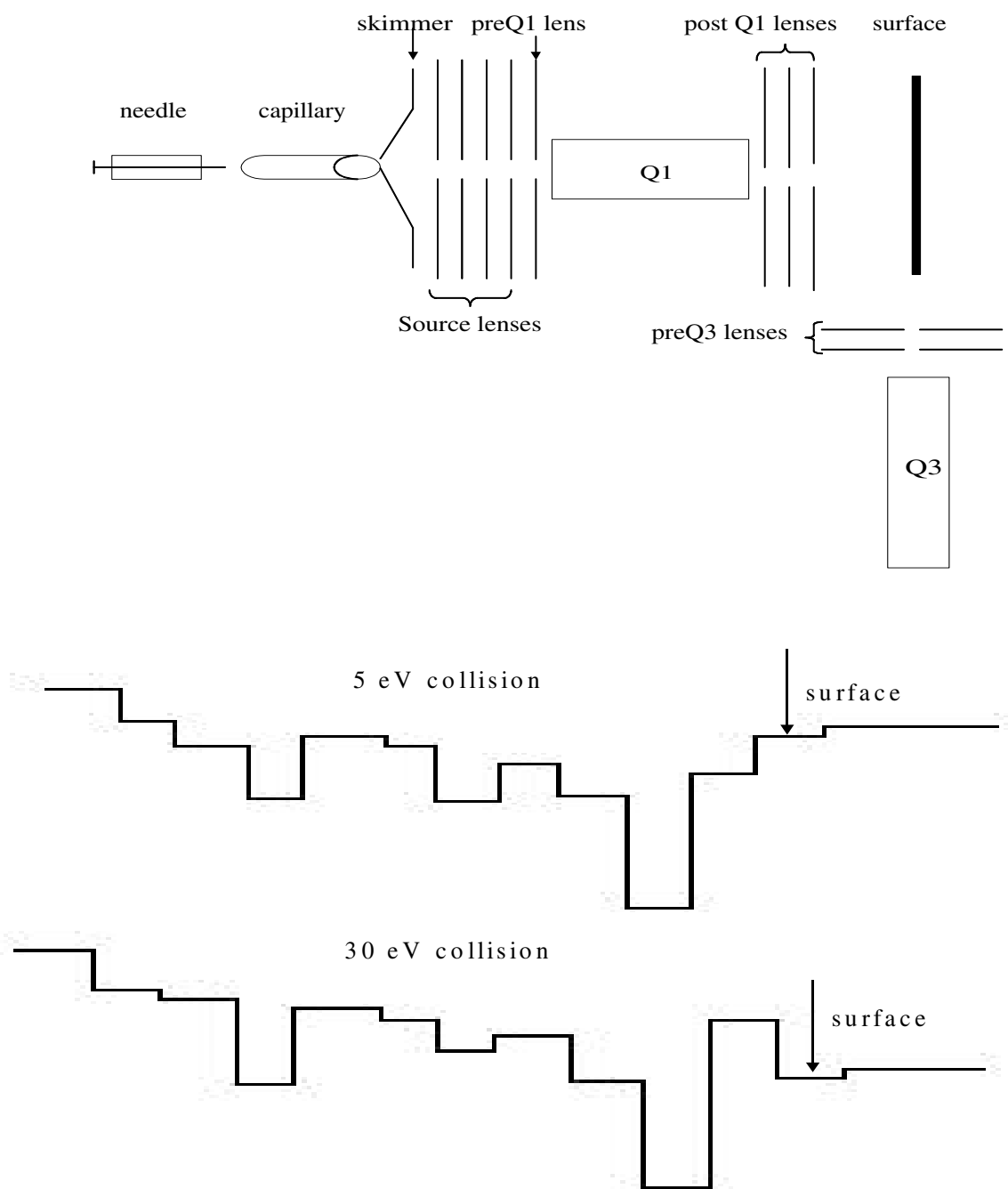
Three different SAM surfaces were used for soft landing, C11OH, C11NH₂, and C12Br. NH₂- and CH₂Br- terminated surfaces are two new surfaces that have never been

employed for soft landing. The C11NH₂ surface was chosen because the NH₂- terminal groups were expected to interact with the C-terminus of the peptide and facilitate the capture of ions in the film matrix. The C12Br surface was employed for comparison with the other surface types; one concern is that the larger mass of the terminal group might result in higher percentages of SID (see Chapter 3). Two different collision energies were applied, 5 eV and 30 eV. Typical lens voltages used in soft landing experiment are listed in Table 1 and shown schematically in Figure 4.1. It should be noted that voltages on the lenses after the surface (preQ3 lenses) are always 4 eV higher than the surface voltage to help focus ions onto the surface. Although most research on soft landing used low collision energies in the range of 1 eV – 10 eV, collision energies as high as 200 eV have been reported.^(122,123) Volny and coworkers soft-landed singly charged gas-phase ions,⁽¹²²⁾ amino acids, peptides, dyes, and protein, on dry metal surfaces at 5-50 eV collision energies. The metal surfaces were oxygen plasma treated and was proposed as the reason for the improved yields of soft landing. Specifically, the metal oxide surface facilitate efficient and nondestructive discharge of ions as well as analyte recovery in the absence of a matrix. A collision energy of 30 eV was used in the current research, in addition to a collision energy of 5 eV, to examine whether the soft landing of a peptide at such a collision energy could be obtained. Even higher collision energies were not used because a significant amount of fragmentation products were observed. Successful soft landing

Table 4.1. Typical lens voltages used in soft landing experiment on the Extrel 4000 instrument.

Lenses	5 eV collision energy	30 eV collision energy
Skimmer	90 V	90 V
Source lens 1	80 V	85 V
Source lens 2	57 V	57 V
Source lens 3	82 V	82 V
Source lens 4	80 V	80 V
Q1 entrance lens	57 V	67 V
Q1 pole bias	75 V	75 V
Q1 exit lens	59 V	59 V
Post Q1 lens 1	-85 V	-70 V
Post Q1 lens 2	67 V	80 V
Surface	85 V	60 V
PreQ3 lens 1	89 V	65 V
PreQ3 lens 2	89 V	65 V
Q3 entrance lens	89 V	65 V
Q3 exit lens	89 V	65 V

Figure 4.1. Schematic diagram demonstration of the lens voltages employed in soft landing experiment at both 5 eV and 30 eV collision energies.



was achieved on all the three SAMs at 30 eV collision energy, but only on C11OH and C11NH₂ surfaces at 5 eV collision energy. The fact that YGGFLR was not soft-landed on the C12Br surface at 5 eV collision energy may be due to the higher surface rigidity, difficulty in ion focusing at such a low collision energy, or poor electrospray efficiency. The MALDI spectra for soft-landed YGGFLR on the C11OH surface at both 5 eV and 30 eV are shown in Figure 4.2.

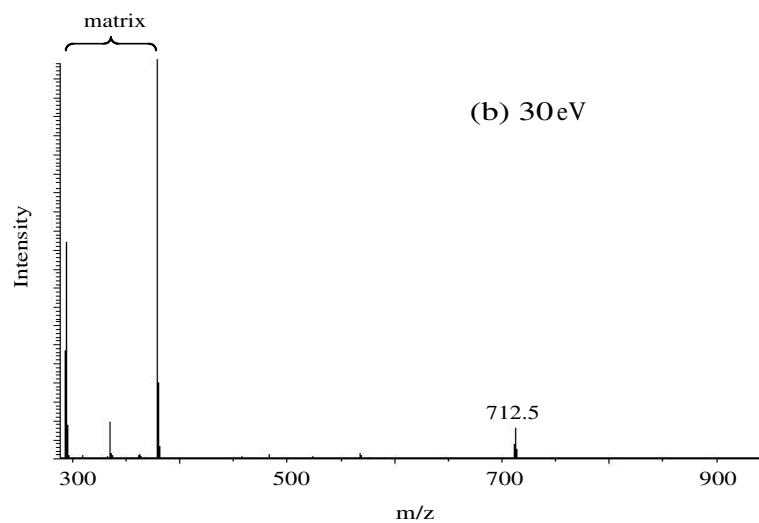
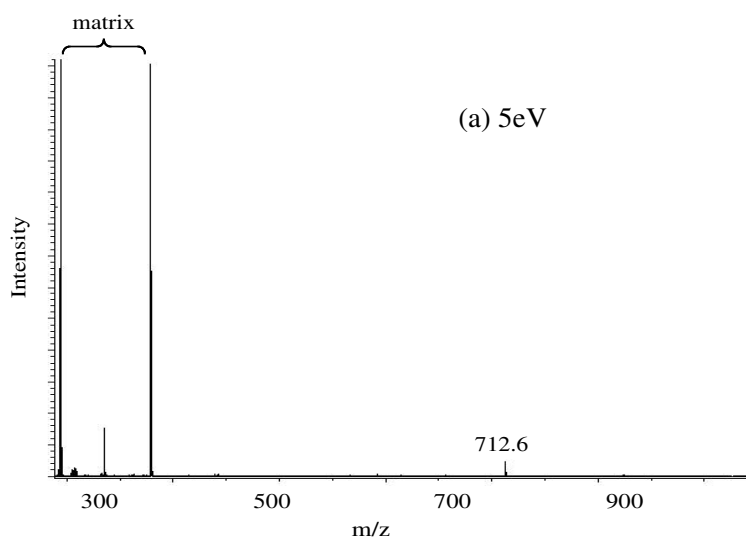
The amount of landed YGGFLR was calculated as described below. A rough approximation of the cross section for YGGFLR was estimated to be $\sim 184.64 \text{ \AA}^2$ using the cross section database on Professor David Clemmer's webpage at Indiana University.⁽¹²⁴⁾ The ion beam diameter was $\sim 5 \text{ mm}$, so the beam area was about 19.62 mm^2 . The number of molecules needed for a monolayer was $\sim 1.06 \times 10^{13}$, the moles needed were $1.77 \times 10^{-11} \text{ mol}$, charges for such amount of singly charged ions was calculated to be $1.70 \times 10^{-6} \text{ C}$, and the time required to form a full monolayer was approximately 473 hrs assuming ion current to be 10^{-12} A . The typical soft landing time in this research was 7hrs, which represents $\sim 1.48\%$ monolayer, and the amount of YGGFLR can be calculated to be 0.187 ng.

4.4 Conclusion

Soft landing of YGGFLR on the C11OH and C11NH₂ surfaces at both 5 eV and 30 eV collision energies was successful. Soft landing of the same peptide on the C12Br surface was only achieved at 30 eV collision energy but not at 5 eV collision energy. This was attributed to the fact that low collision energy can cause difficulty in ion focusing and subsequent ion loss but because it only happened with the C12Br surface it must be

assumed that the terminal group mass/surface rigidity or interface dipole of this surface rendered its behavior different from the other two surfaces.. The deposited amount of peptide was calculated to be in the tenths of a nanogram range. Further optimization of the ion optics voltages and the electrospray efficiency needs to be done to shorten the deposition time. There remains much that can be done to explore the applications of the soft landing technique, which will be described in Chapter 5.

Figure 4.2 MALDI spectra for YGGFLR soft-landed on a C11OH surface at (a) 5 eV and (b) 30 eV and subsequently collected by a solvent rinse. The peak at m/z 712 is the $(\text{YGGFLR} + \text{H})^+$ ion, peaks at lower m/z range are matrix peaks.



Chapter 5 Summary and Future Directions

Low energy ion-surface collisions have been demonstrated to be a useful tool for probing both the property and structure of organic thin films and the reactivity of the polyatomic ions. Self-assembled monolayers with systematically changing halogen terminal groups have been shown to be good model surfaces for SID study, and the electronic and reactive behavior of the monolayer was illustrated and characterized with several small organic probe ions.

The conversion of kinetic energy to internal energy on all surfaces decreases in the order of $C_{12}Br > C_{12}F_{10} > C_{14}F_1 \approx C_{12}Cl > C_{12}$ for both benzene and $W(CO)_6$ projectile ions. The energy deposition order can be linearly related to the mass of the terminal group, CH_2Br (94) $>$ CF_3 (69) $>$ CH_2Cl (49) $>$ CH_3 (15), so the terminal mass is believed to be the dominant factor in determining the energy deposition. $W(CO)_6$ projectile ions show lower internal energy deposition than benzene ions on all of the surfaces studied. This can be attributed to the lower first appearance energy (1.2 eV) of $W(CO)_6$ ions compared with that of the benzene ions (4.6 eV) leading to a greater excess internal energy in benzene prior to surface collision. These two projectiles show similar energy deposition after correcting for the first appearance energy difference. Electron transfer through the organic thin films has also been studied. Neutralization of the incoming ions increases in the order of $C_{12}F_{10} < C_{14}F_1 < C_{12}Cl < C_{12}Br < C_{12}$, which has a good exponential relationship with the interface dipoles but not the ionization

energy of the films. As a conclusion, electron transfer is mainly determined by the interface dipole of the surface.

Ion-surface reactions were observed on all SAM films. Specifically, fluorine addition products ($C_6H_6^+ + F - H = C_6H_5F^+$ (m/z 96) and $C_6H_6^+ + F - H_2 = C_6H_4F^+$ (m/z 95)) were detected on C12F10 and C14F1 surfaces with benzene molecular ion, and hydrogen addition products ($C_7H_7^+$ (m/z 91)) were seen on all surfaces except C12F10 surface. When pyrazine was used as the projectile, reactions occur between the pyrazine ions and the available hydrogen atoms to form $C_4N_2H_4^+ + H = C_4N_2H_5^+$ (m/z 81) ions which was observed on C14F1, C12Cl, C12Br and C12 surfaces. The fact that hydrogen addition products were observed on C14F1 but not C12F10 surface can be attributed to the hydrogen abstraction from underlying $(CH_2)_n$ chains. No reaction product resulting from Cl abstraction from C12Cl surface or Br abstraction from C12Br surface was detected but this does not rule out the possibility of Br^- or Cl^- abstraction which could produce neutral CD_3Cl or CD_3Br and an ionized chain.

Future studies may involve the use of large projectiles with higher molecular weight and different structures, for example, peptides and proteins, to investigate above processes and compare with small projectile ions. Surfaces with terminal groups containing two or three Cl or Br atoms ($CHCl_2$, CCl_3 , $CHBr_2$, CBr_3 terminal groups) can be synthesized and used for SID study. The approximately doubled or tripled terminal mass is expected to increase the energy transfer on these surfaces significantly which will be very useful for the fragmentation of large biomolecules. These studies will definitely

add to our fundamental understanding of the complicated processes of ion-surface collision.

A peptide, YGGFLR, was used to perform soft landing on C11OH, C11NH₂, and C12Br self-assembled monolayer films. Two different collision energies were employed, 5 eV and 30 eV. The former is in the commonly used energy range (1 – 13 eV) and successful soft landing was achieved on both C11OH and C11NH₂ surfaces but not on C12Br surfaces. The latter energy was tried since it has reported that collision energy as high as 200 eV could be employed for soft landing experiments. At 30 eV collision energy, successful soft-landing was obtained on all of the three surfaces. The fact that YGGFLR could be soft-landed on the C12Br surface at 30 eV but not at 5 eV collision energy suggests that low collision energy results in difficulty in ion focusing for this surface and thus lost of ions. In the future, peptides of larger size and proteins of different structures will be soft-landed to optimize the electrospray condition and lens voltages and shorten the time needed for soft landing. Quantification of the soft-landed materials by MALDI will help to determine the shortest time required for the minimal detectable amount. Dyes and fluorescent compounds will be soft landed on different surfaces to demonstrate a directly visible confirmation of deposited materials. Structures of special interest in peptide and protein fragmentation, such as diketopiperazine vs. oxazalone b ion standards can be formed in the source region and be separated and then soft-landed on surface for further analysis. In addition, material related compounds with very similar structures that are hard to separate by conventional chromatography can be separated by their different masses and collected by soft landing. Protein arrays might also be formed

on specific locations on patterned SAMs formed by micro-contact printing. Another exciting experiment to try is the direct analysis of the soft-landed compound without rinsing and concentrating steps which results in sample loss. Direct analysis will be done by fixing the soft-landed surface on a plain MALDI sample plate (no sample well) which will be loaded into the MALDI-TOF instrument for analysis or by sputtering performed directly in the same chamber as the soft-landing.

REFERENCES:

1. McLafferty, F.W. *Interpretation of Mass Spectra*, 4th Edition. University Science books, Mill Valley, **1993**
2. Levsen, K. *Fundamental Aspects of organic Mass Spectrometry*. Verlag Chemie, New York, **1978**
3. Sleno, L.; Volmer, D.A. *J. Mass spectrum*. **2004**, 39, 1091
4. Shukla, A.K.; Futrell, J.H. *J. Mass. Spectrom.* **2000**, 35, 1069
5. Jennings K.R. *Int. J. Mass Spectrom.* **2000**, 200, 479
6. Schwartz R.N.; Slawsky, Z.I.; Herzfeld, K.F. *J. Chem. Phys.* **1952**, 20, 1591
7. Cooks, R.G.; Ast, T.; Beynon, J.H. *Int. J. Mass. Spectrom. Ion Phys.* **1975**, 16, 348
8. Cooks, R.G.; Ast, T.; Mabud, M.A. *Int. J. Mass. Spectrom. Ion Processes* **1990**, 100, 209
9. Kleinnijenhuis, A.J.; Heck, A.J.R.; Duursma, M.C. *et al. J. Am. Soc. Mass Spectrom.* **2005**, 16(10), 1595
10. Moore, D.T.; Oomens, J.; Eyler, J.R. *et al. J. Am. chem. Soc.* **2005**, 127 (19), 7243
11. Wang, W.J.; Kitova, E.N.; Sun, J.X. *et al. J. Am. Soc. Mass Spectrom.* **2005**, 16(10), 1583
12. Mabud, Md.A.; DeKrey, M.J.; Cooks, R.G. *Int. J. Mass Spectrom. Ion Proc.* **1985**, 67, 285
13. DeKrey, M.J.; Mabud, Md.A.; Cooks, R.G.; Syka, J.E.P. *Int. J. Mass Spectrom. Ion Proc.*, **1985**, 67, 295
14. Mabud, Md.A.; Ast, T.; Cooks, R.G. *Org. Mass Spectrom.* **1987**, 22, 418
15. Bier, M.E.; Amy, J.W.; Cooks, R.G.; Syka, J.E.P.; Ceja, P.; Stafford, G. *Int. J. Mass Spectrom. Ion Proc.* **1987**, 77, 31
16. DeKrey, M.J.; KenttEmaa, H.I.; Wysocki, V.H.; Cooks, R.G. *Org. Mass Spectrom.* **1986**, 21, 193

17. Gamage, C.M.; Fernandez, F.M.; Kuppanan, K.; Wysocki, V.H. *Anal. Chem.* **2004**, *76*(17), 5080
18. Dongre, A.R.; Jones, J.L.; Somogyi, A.; Wysocki, V.H. *J. Am. Chem. Soc.* **1996**, *118*(35), 8365
19. Dongre, A.R.; Somogyi, A.; Wysocki, V.H. *J. Mass. Spectrom.* **1996**, *31*(4), 339
20. Lakins, J.; Denisov, E.; Futrell, J. *J. phys. Chem. B* **2001**, *105*, 1895
21. Bosio, S.B.M.; Hase, W.L. *Int. J. Mas Spectrom. Ion Processes* **1998**, *174*, 1
22. Yan, T.; Isa, N.; Gibson, K.D.; Sibener, S.J.; Hase, W.L. *J. Phys. Chem. A* **2003**, *107*, 10600
23. Wijesundara, M.B.J.; Fuoco, E.; Hanley, L. *Langmuir* **2001**, *17* (19), 5721-5726
24. Schultz, D.G.; Lim, H.; Garbis, S.; Hanley, L. *J. Mass Spectrom.* **1999**, *34*, 217
25. Williams, E.R.; Henry, K.D.; McLafferty, F.W.; Shabanowitz, J.; Hunt, D.F. *J. Am. Soc. Mass Spectrom.* **1990**, *1*, 413
26. Chorush, R.A.; Little, D.P.; Beu, S.C.; Wood, T.D.; McLafferty, F.W. *Anal. Chem.* **1995**, *67*, 1042
27. Beck, R.D.; St. John, P.; Homer, M.L.; Whetten, R.L. *Science*, **1991**, *253*, 879
28. St. John, P.; Beck, R.D.; Whetten, R.L. *Phys. Rev. Lett.* **1992**, *69*, 1467
29. Ijames, C.F.; Wilkins, C.L. *Anal. Chem.* **1990**, *62*, 330
30. Castoro, J.A.; Nuwaysir, L.M.; Ijames, C.F.; Wilkins, C.L. *Anal. Chem.* **1992**, *64*, 2238
31. Wysocki, V.H.; Ding, J.M.; Jones, J.L.; Callahan, J.H.; King, F.L. *J. Am. Soc. Mass. Spectrom.* **1992**, *3*, 27
32. Wysocki, V.H.; Kenttämaa, H.; Cooks, R.G. *Int. J. Mas Spectrom. Ion Process.* **1987**, *75*, 181
33. Jones, J.L.; Dongré, A.R.; Somogyi, Á.; Wysocki, V.H. *J. Am. Chem. Soc.* **1994**, *116*, 8368

34. Wysocki, V.H.; Tsapraillis, G.; Smith, L.L.; Brechi, L.A. *J. Mass. Spectrom.* **2000**, *35*, 1399
35. Schaaff, T.G.; Qu, Y.; Farrell, N.; Wysocki, V.H. *J. Mass. Spectrum.* **1998**, *33*, 436
36. Wong S.C.; Lockyer, N.P.; Vickerman, J.C. *Surface and interface analysis* **2005**, *37(9)*, 721
37. Piwonski, I.; Grobelny, J.; Cichomski, M.; Celichowski, G.; Rogowski, J. *Applied surface science* **2005**, *242 (1-2)*, 147
38. Ouyang, Z.; Takats, Z.; Blake, T.A. *et al. Science* **2003**, *301*, 1351
39. Miller, S.A.; Luo, H.; Pachuta, S.J.; Cooks, R.G. *Science* **1997**, *275*, 1447
40. Vékey, K.; Somogyi, Á.; Wysocki, V.H., *J. Mass Spectrom.* **1995**, *30*, 212
41. Smith, D.L.; Wysocki, V.H.; Colorado, R., Jr.; Shmakova, O.E.; Graupe, M.; Lee, T.R. *Langmuir* **2002**, *18*, 3895
42. Morris, M.R.; Riederer, D.E.; Winger, B.E.; Cooks, R.G.; Ast, T.; Chidsey, C.E. D. *Int. J. Mass Spectrom. Ion. Progresses* **1992**, *122*, 181
43. Miller, S.A.; Riederer, E.; Cooks, R.G.; Cho, W.R.; Lee, H.W.; Kang, H., *J. Phys. Chem.* **1994**, *98*, 245
44. Kane, T.E.; Wysocki, V.H. *Int. J. Mass Spectrom. Ion processes* **1994**, *140*, 177
45. Somogyi, Á; Smith, D.L.; Wysocki, V.H.; Colorado, R. Jr.; Lee, T.R. *J. Am. Soc. Mass Spectrom.* **2002**, *13*, 1151
46. Alloway, D.M.; Hoftmann, M.; Smith, D.L.; Gruhn, N.E.; Graham, A.L.; Colorado, R. Jr.; Wysocki, V.H.; Lee, T.R.; Lee, P.A.; Armstrong, N.R. *J. Phys. Chem. B* **2003**, *107*, 11690
47. Somogyi, Á; Kane, T.E.; Ding, M.J.; Wysocki, V.H. *J. Am. Chem. Soc.* **1993**, *115*, 5275
48. Cooks, R.G.; Ast, T.; Pradeep, T., Wysocki, V.H. *Acc. Chem. Res.* **1994**, *27*, 316
49. Gu, C. G.; Wysocki, V. H. *J Am. Chem. Soc.* **1997**, *119*, 12010
50. Gu, C.G.; Wysocki, V.H.; Harada, A.; Takaya, H.; Kumadaki, I. *J. Am. Chem.. Soc.* **1999**, *121*, 10554

51. Angelico, V.J.; Mitchell, S.A.; Wysocki, V.H. *Anal. Chem.* **2000**, *72*, 2603
52. Vincenti, M.; Cooks, R.G. *Organic Mass Spectrometry* **1988**, *23*, 317
53. Schreiber, F. *Progress in Surface Science* **2000**, *65*, 151
54. Flinklea, H.O. *Encyclopedia of analytical chemistry: Applications, Theory and Instrumentation*, Wiley & Sons, New York, **2000**
54. Nuzzo, R.G.; Korenic, E.M.; Dubois, J. *Chem. Phys.* **1990**, *93*, 767
55. Prathima, N.; Harini, M.; Rai, N. *et al. Langmuir* **2005**, *21*, 2364
57. Barrena, E.; Palacios-Lidon, E.; Munuera, C. *et al. J. Am. Chem. Soc.* **2004**, *126*, 385
56. Van Alsten, J.G. *Langmuir* **1999**, *15*, 7605
57. Kidoaki, S.; Matsuda, T. *Langmuir* **1999**, *15*, 7639
58. Davis, F.; Higson, S. *Biosensors and Bioelectronics* **2005**, *21(1)*, 1
59. Senaratne, W.; Andruzzi, L.; Ober, C.K. *Biomacromolecules* **2005**, *6(5)*, 2427
60. Chaki, N.K.; Vijayamohan, K. *Biosensors and Bioelectronics* **2002**, *17(1-2)*, 1
61. Fendler, J.H. *Chemistry of Materials* **2001**, *13(10)*, 3196
62. Bumm, L.A.; Arnold, J.J.; Cygan, M.T. *et al. Science* **1996**, *271*, 1705
63. Leatherman, G.; Durantini, E.N.; Gust, D. *et al. J. Phys. Chem. B* **1999**, *103*, 4006
64. Jirage, K.B.; Hulteen, J.C.; Martin, C.R. *Science* **1997**, *278*, 655
65. Santhanam, V.; Andres, R.P. *Nano Lett.* **2004**, *4*, 41
66. Love, J.C.; Estroff, L.A.; Kriebel, J.K.; Nuzzo, R.G.; Whitesides, G.M. *Chem. Rev.* **2005**, *105*, 1103
67. Bain, C.D.; Troughton, E.B.; Tao, Y.T.; Evall, J.; Whitesides, G.M.; Nuzzo, R.G.; *J. Am. Chem. Soc.* **1989**, *111*, 321
68. Porter, M.D.; Bright, T.B.; Allara, D.L.; Chidsey, C.E.D. *J. Am. Chem. Soc.* **1987**, *109*, 3559

69. Alves, C.A.; Smith, E.L.; Porter, M.D. *J. Am. Chem. Soc.* **1992**, *114*, 1222
70. Camillone, N.; Chidsey, C.E.D.; Liu, G.Y.; Putvinski, T.M.; Scoles, G. *J. Chem. Phys.* **1991**, *94*, 8493 Schreiber, F. *Prog. Surf. Sci.* **2000**, *65*, 151
71. Poirier, G.E. *Chem. Rev.* **1997**, *97*, 1117
72. Poirier, G.E. *Langmuir* **1997**, *13*, 2019
73. Zhang, L.; Goddard, W.A. III; Jiang, S. *J. Chem. Phys.* **2002**, *117*, 7342
74. Ulman, A. *Chem. Rev.* **1996**, *96*, 1533
75. Yourdshahyan, Y.; Rappe, A.M. *J Chem Phys.* **2002**, *117*, 825
76. Kim, H.I.; Koini, T.; Lee, T.R.; Perry, S.S. *Langmuir* **1997**, *13*, 7192
77. Gu, C. Ph.D. Dissertation; University of Arizona: Tucson, AZ, **1999**.
78. Skoog, D.A.; Holler, F.J.; Nieman, T.A. *Principles of Instrumental Analysis*. Fifth ed. Thomson learning, **1997**
79. Nebesny, K.W.; Maschhoff, B.L.; Armstrong, N.R. *Anal. Chem.* **1989**, *61*, 469A
80. Kratos Analytical. <http://www.kratos.com/Agen/SMA.html>
81. Lichtenberger, D.L.; Kellogg, G.E.; Kristofzski, J.G. *et al. Rev. Sci. Instrum.* **1986**, *57*, 2366
82. http://www.ksvinc.com/contact_angle.htm
83. Graupe, M.; Takenaga, M.; Koini, T.; Colorado, R.Jr; Lee, T.R. *J. Am. Chem. Soc.* **1999**, *121*, 3222
84. Colorado, R. Jr; Lee, T.R. *J. Phys. Org. Chem.* **2000**, *13*, 796
85. Folkers, J.P.; Laibinis, P.E.; Whitesides, G.M. *Langmuir* **1992**, *8*, 1330
86. Cary, F.A.; *15.13. Preparation of Thiols*; 2nd, McGraw-Hill Inc. New York, **1992**, pp619
87. Kim, D.S.; Lee, Y.H. *Thin solid films* **1996**, 283, 109

88. Ada, E.T.; Lee, S.M.; Lee, H.; Rabailais, J.W. *J. Phys. Chem. B* **2000**, *104*, 5132
89. Smith, D.L.; Selven, R.; Wysocki, V.H. *Langmuir* **2003**, *19*, 7302
90. Laskin, J.; Futrell, J.H. *J. Chem. Phys.* **2003**, *119*(6), 3413
91. Wu, Q.; Hanley, L. *J. Am. Chem. Soc.* **1993**, *115*, 1191
92. John, P.M.; Whetten, R.L. *Chem. Phys. Lett.* **1992**, *196*, 330
93. Kane, T.E.; Somogyi, A.; Wysocki, V.H. *Org. Mass Spectrom.* **1993**, *28*, 1665
94. Winger, B.E.; Julian, .K.; Cooks, R.G.; Chidsey, C.E.D. *J. Am. Chem. Soc.* **1991**, *113*, 8967
95. Wysocki, V.H.; Jones, J.L.; Ding, J.M. *J. Am. Chem. Soc.* **1991**, *113*, 8969
96. Busmann, H.G.; Lill, Th.; Reif, B.; Hertel, I.V.; Maguir, H.G. *J. Chem. Phys.* **1993**, *98*, 7574
97. Meroueh, O.; Hase, W.L. *Phys. Chem. Chem. Phys.*, **2001**, *3*, 2306
98. Cohen, S.R.; Naaman, R.; Sagiv, J. *Phys. Rev. Lett.* **1987**, *58*(12), 1208
99. Lemoine, D.; Quattrucci, J.G.; Jackson, B. *Phys. Rev. Lett.* 2002, *89*(26), 268302
100. Snyder, R. G.; Schachtsneider, J. H. *Spectrochimica Acta* **1963**, *19*, 85
101. Macphail, R. A.; Strauss, H. L.; Snyder, R. G.; Elliger, C. A. *J. Phys. Chem.* **1982**, *88*, 334
102. Cai, M.; Ho, M.; Pemberton, J. E. *Langmuir* **2000**, *16*, 3446
103. Snyder, R. G.; Strauss, H. L.; Elliger, C. A. *J. Phys. Chem.* **1982**, *86*, 5145
104. Folkers, J.P.; Laibinis, P.E.; Whitesides, G.M. *Langmuir* **1992**, *8*, 1330
105. Folkers, J.P.; Laibinis, P.E.; Whitesides, G.M.; Deutch, J. *J. Phys. Chem.* **1994**, *98*, 563
106. Bain, C.D.; Evall, J.; Whitesides, G.M. *J. Am. Chem. Soc.* **1989**, *111*, 7155
107. Bunn, C.W.; Howells, E.R. *Nature*, **1954**, *174*, 579

108. Fan, F.F.; Yang, J.; Cai, L. *et al. J. Am. Chem. Soc.* **2002**, *124*, 5550
109. Cardona, M.; Ley, L.; Eds. *Photoemission in Solids I*: SpringerVerlag: New York, **1978**
110. Luo, H.; Miller, S.A.; Cooks, R.G.; Pachuta, S.J. *Int. J. Mass Spectrom. Ion processes* **1998**, *174*, 193
111. Geiger, R.J.; Melnyk, M.C.; Busch, K.L.; Bartlett, M.G. *Int. J. Mass Spectrom.* **1999**, *182/183*, 415
112. Bromann, K.; Felix, C.; Brune, H. *et al. Science*, **1996**, *274*, 956
113. Kitching, K.J.; Lee, H.N.; Elam, W.T. *et al. Rev. Sci. Instrum.* **2003**, *74*, 4832
114. Feng, B.B.; Wunschel, D.S.; Masselon, C.D.; Pasa-Tolic, L.; Smith, R.D. *J. Am. Chem. Soc.* **1999**, *121*, 8961
115. Fenselau, C.; Demirev, P.A. *Mass Spectrom. Rev.* **2001**, *20*, 157
116. Blake, T.A.; Ouyang, Z.; Wiseman, J.M. *et al. Anal. Chem.* **2004**, *76*, 6293
117. Gologan, B.; Takats, Z.; Alvarez, J. *et al. J. Am. Soc. Mass Spectrom.* **2004**, *15*, 1874
118. Shen, J.; Yim, Y.H.; Feng, B. *et al. Int. J. Mass Spectrom.* **1999**, *182/183*, 423
119. Back, J.F.; Oakenfull, D.; Smith, M.B. *Biochemistry* **1979**, *18*, 5191
120. Volny, M.; Elam, W.T.; Ratner, B.; Turecek, F. *Anal. Chem.* **2005**, *77*, 4846
121. Volny, M.; Elam, W.T.; Branca, A.; Ratner, B.; Turecek, F. *Anal. Chem.* **2005**, *77*, 4890
122. <http://www.indiana.edu/~clemmer/>